nature aging

Article

https://doi.org/10.1038/s43587-023-00460-8

Impaired BCAA catabolism in adipose tissues promotes age-associated metabolic derangement

Received: 16 July 2022

Accepted: 27 June 2023

Published online: 24 July 2023

Check for updates

Hye-Sook Han[1,12], Eunyong Ahn[2,12], Eun Seo Park[3,12], Tom Huh[1], Seri Choi[1], Yongmin Kwon[1], Byeong Hun Choi[1], Jueun Lee[2], Yoon Ha Choi[4], Yujin L. Jeong[4], Gwang Bin Lee[5], Minji Kim[6,7,8], Je Kyung Seong[9], Hyun Mu Shin[7,8,10], Hang-Rae Kim[6,7,8,10], Myeong Hee Moon[5], Jong Kyoung Kim[3,4] ✉, Geum-Sook Hwang[2,11] ✉ & Seung-Hoi Koo[1] ✉

Adipose tissues are central in controlling metabolic homeostasis and failure in their preservation is associated with age-related metabolic disorders. The exact role of mature adipocytes in this phenomenon remains elusive. Here we describe the role of adipose branched-chain amino acid (BCAA) catabolism in this process. We found that adipocyte-specific *Crtc2* knockout protected mice from age-associated metabolic decline. Multiomics analysis revealed that BCAA catabolism was impaired in aged visceral adipose tissues, leading to the activation of mechanistic target of rapamycin complex (mTORC1) signaling and the resultant cellular senescence, which was restored by *Crtc2* knockout in adipocytes. Using single-cell RNA sequencing analysis, we found that age-associated decline in adipogenic potential of visceral adipose tissues was reinstated by *Crtc2* knockout, via the reduction of BCAA–mTORC1 senescence-associated secretory phenotype axis. Collectively, we propose that perturbation of BCAA catabolism by CRTC2 is critical in instigating age-associated remodeling of adipose tissue and the resultant metabolic decline in vivo.

Age-associated metabolic derangement is detrimental in prolonging healthspan. Adipose tissues are critical in regulating whole-body energy metabolism and the impairment of their function during the aging process could be one of the main causes for the dysregulation of energy homeostasis[1–3]. The predominant parenchymal cells in adipose tissues are adipocytes in white adipose tissue (WAT), especially in visceral white adipose tissue (VAT), which are mainly responsible for the storage of triacylglycerols (TAGs), whereas adipocytes in brown adipose tissue (BAT) and beige adipocytes in subcutaneous WAT (SAT) are critical in maintaining energy balance by functioning as major players for adaptive thermogenesis[4]. Age-dependent increases in visceral adiposity could lead to chronic inflammation and resultant insulin resistance, leading to the progression of metabolic disorders that deteriorate the overall health of individuals, leading to reduced life expectancy.

[1]Division of Life Sciences, Korea University, Seoul, Korea. [2]Integrated Metabolomics Research Group, Western Seoul Center, Korea Basic Science Institute, Seoul, Korea. [3]Department of New Biology, DGIST, Daegu, Korea. [4]Department of Life Sciences, POSTECH, Pohang, Korea. [5]Department of Chemistry, Yonsei University, Seoul, Korea. [6]Department of Anatomy & Cell Biology, Seoul National University College of Medicine, Seoul, Korea. [7]Department of Biomedical Sciences, Seoul National University College of Medicine, Seoul, Korea. [8]BK21 FOUR Biomedical Science Project, Seoul National University College of Medicine, Seoul, Korea. [9]Korea Mouse Phenotyping Center, Seoul National University, Seoul, Korea. [10]Wide River Institute of Immunology, Seoul National University, Hongcheon, Korea. [11]College of Pharmacy, Chung-Ang University, Seoul, Korea. [12]These authors contributed equally: Hye-Sook Han, Eunyong Ahn, Eun Seo Park. ✉e-mail: blkimjk@postech.ac.kr; gshwang@kbsi.re.kr; koohoi@korea.ac.kr

Adipose tissues are composed of multiple cell types, including mature adipocytes, adipogenic progenitor (AP) cells, endothelial cells and various types of immune cells[5]. At the cellular level, age-associated decline in functional adipose tissues can be instigated by cellular senescence. Specifically, cellular senescence of AP cells has been extensively studied. Obesity-induced metabolic dysfunction was associated with the increased cellular senescence of AP cells in WAT, via senescence-associated secretory phenotype (SASP) factor-mediated inhibition of adipogenesis and accumulation of macrophages[6]. Indeed, clearance of senescent AP cells improved metabolic disorders in obese mice, suggesting that senescence-associated metabolic complications can be reversed. Similarly, age-dependent accumulation of senescent AP cells in adipose tissues led to the increased expression of SASP factors, including activin A, which promotes the formation of dysfunctional adipose tissues[7–9]. These data suggest that secretion of SASP from senescent cells in adipose tissues is critical in the instigation of age-associated metabolic decline of adipose tissues via an autocrine and/or paracrine manner. Given the potential crosstalk between the multiple cell types in adipose tissues, the exact mechanism by which distinct cells influence age-associated progression of dysfunctional adipose tissues needs to be delineated.

cAMP-response element-binding protein (CREB) regulated transcription coactivator (CRTC) 2 is involved in the regulation of metabolic homeostasis[10]. We and others showed that CRTC2 regulates hepatic gluconeogenesis by co-activating basic leucine zipper (bZIP) transcription factors such as CREB, CREBH and activating transcription factor 6 (refs. 11–13). Furthermore, CRTC2 regulates hepatic lipid metabolism by counteracting the actions of Sterol regulatory element-binding proteins (SREBPs)[14,15]. Recently, we have shown that CRTC2 transcriptionally induces hepatic expression of miR-34a under diet-induced obesity, resulting in the progression of fatty liver and insulin resistance[16,17]. In addition, CRTC2 also regulates the production of endocrine hormones in pancreatic β-cells and intestinal L cells[18,19]. Although the role of CRTC3 in adipose tissues has been delineated recently[20,21], the exact function of adipose CRTC2 has yet to be tested by using tissue-specific knockout mice.

Notably, CRTC-1, an ortholog of CRTCs found in *Caenorhabditis elegans*, was shown to be associated with aging and aging-related disorders. AMP-activated protein kinase (AMPK) inhibits CRTC-1 activity to increase lifespan of *C. elegans*, suggesting that inhibition of CRTC-1 could be beneficial in combating aging-related disorders[22]. Indeed, deletion of CRTC-1 enhanced lifespan of this organism by improving mitochondrial function[22,23]; however, the role of CRTCs in mammals in aging or age-associated metabolic disorders has not been delineated.

Here we investigated the role of adipose CRTC2 in age-associated metabolic dysregulation. We found that expression of adipose CRTC2 was elevated upon aging in VAT. Age-mediated increases in adiposity were substantially reduced in adipocyte-specific *Crtc2* knockout (*Crtc2* AKO) mice compared to the control, leading to the protection from age-associated metabolic disorders. Mechanistically, depletion of *Crtc2* in adipocytes enhanced the sirtuin (SIRT) 1/AMPK pathway and reduced mechanistic target of rapamycin complex (mTORC) 1 pathway via the regulation of BCAA catabolism, leading to the preservation of mitochondria and the reduction in cellular senescence in VAT. Using single-cell RNA sequencing (scRNA-seq), we found that age-mediated remodeling of adipose tissue architecture was prevented upon *Crtc2* knockout in adipocytes, in part via the reduction of SASP factors. Indeed, adipogenic potential of AP cells from the aged *Crtc2* AKO mice is comparable to those from young wild-type (WT) mice. These data suggest that CRTC2 in mature adipocytes is critical in the progression of age-associated metabolic decline in VAT by promoting cellular senescence in mammals.

Results

Deleting adipose *Crtc2* averts age-related metabolic disorder

To explore the potential role of CRTC2 in age-associated metabolic decline of adipose tissues, we first attempted to determine the relative CRTC2 expression in adipose tissues. Notably, we observed that CRTC2 expression is more than tenfold enriched in WAT compared to BAT (Extended Data Fig. 1a). Among WAT, expression of CRTC2 is slightly higher in VAT than in SAT. Furthermore, we observed a significant increase in CRTC2 protein levels in response to aging in mature adipocytes from VAT but not from SAT. We were not able to detect CRTC2 expression in mature adipocytes from BAT. These data prompted us to generate adipocyte-specific *Crtc2* knockout (*Crtc2* AKO) mice and look for the potential role of CRTC2 mainly in VAT in response to aging (Extended Data Fig. 1b). We confirmed that *Crtc2* AKO mice showed reduced expression of CRTC2 in adipose tissues, but not in other tissues (Extended Data Fig. 1c,d).

To explore the potential role of adipose CRTC2 in response to aging, we chose specific age groups for the study. For C57BL/6 mice, the aged group is considered to be at the age of 18–24 months (human age equivalents to 56–69 years), whereas the mature adult group falls within 3–6 months in age (human age equivalents to 20–30 years)[24]. Thus, we chose 18–21-month-old mice as the aged group, while selecting 3–5-month-old mice as their younger counterparts. As expected, aged WT mice displayed pronounced age-associated metabolic anomalies, including glucose and insulin intolerance, increased fat body mass and an increased lipid accumulation in liver and adipose tissues compared to the younger counterparts (Fig. 1a–g). Of note, aged *Crtc2* AKO mice showed a resistance to the age-associated metabolic decline, as shown by the reduced adiposity and the improved glucose homeostasis that were comparable to the younger WT mice (Fig. 1a–g and Extended Data Fig. 1e). On the other hand, we did not observe the effect of adipocyte-specific depletion of *Crtc2* on metabolism in the 3-month-old group, except a slight reduction of overnight-fasting blood glucose levels (Supplementary Fig. 1). These data suggest that adipose CRTC2 may play more prominent roles in older age groups. Age-associated decline in SAT:VAT ratio is often correlated with the metabolic disorder. Indeed, we observed that SAT:VAT ratio was dramatically reduced by aging, which was partially recovered by adipocyte-specific depletion of *Crtc2* (Fig. 1h). Although the age-associated decrease in energy expenditure was not recovered by adipose *Crtc2* knockout (Supplementary Fig. 2), peripheral insulin signaling was improved in aged *Crtc2* AKO mice compared to the aged WT controls (Extended Data Fig. 2a,b), which is in line with the results of the insulin tolerance test (Fig. 1b). Again, adipocyte-specific depletion of *Crtc2* in young mice did not show differences in insulin signaling (Extended Data Fig. 2c,d). These data suggest that adipocyte-specific depletion of *Crtc2* could reverse the age-associated metabolic disorders mainly by changing yet-to-be-specified aspects of signaling cascades in VAT.

Aged *Crtc2* AKO mice display improved lipid homeostasis

Having seen a dramatic effect of aging on adiposity, we then wanted to further elaborate the effect of aging and *Crtc2* knockout in lipid metabolism. We mainly focused on liver and VAT, which are major organs for controlling lipid homeostasis in mammals.

Hepatic lipid contents were increased in aged WT mice compared to young WT controls, in line with the increased adiposity caused by aging (Fig. 1d,g). Adipocyte-specific depletion of *Crtc2* reduced lipid accumulation in liver that was induced by aging, showing a systemic anti-aging effect by adipocyte-specific depletion of *Crtc2*. To further assess the effect of aging and/or adipocyte-specific depletion of *Crtc2* on hepatic lipid metabolism, we performed lipidomics analysis.

A principal component analysis (PCA) showed differences in quantified hepatic lipid profiles ($P < 0.05$) among the three groups (young WT mice, aged WT mice and aged *Crtc2* AKO mice), although the difference between young WT mice and aged WT mice might be more

https://doi.org/10.1038/s43587-023-00460-8

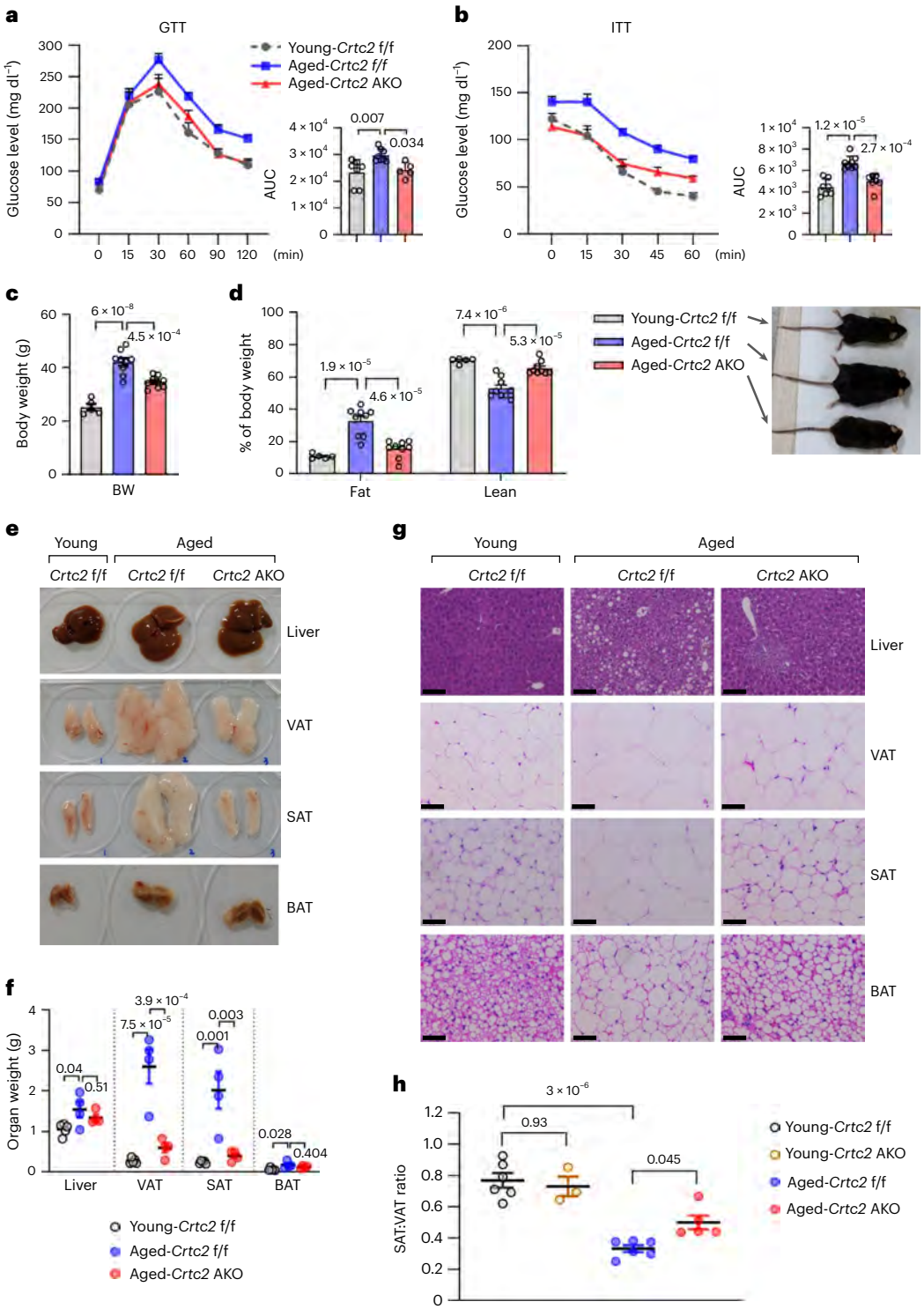

Fig. 1 | Adipocyte-specific depletion of Crtc2 suppresses the age-onset metabolic disorder in mice. The metabolic phenotypes of male young *Crtc2* f/f mice (3 months old), aged *Crtc2* f/f mice (18 months old) and aged *Crtc2* AKO mice (18 months old) were assessed. **a**, A glucose tolerance test (GTT) was performed on mice. Blood glucose levels at the designated time points are shown (left). The area under the curve (AUC) was calculated for the glucose tolerance test for each mouse (right). Data represent mean ± s.d. ($n = 7$ for young *Crtc2* f/f mice; $n = 8$ for aged *Crtc2* f/f mice; and $n = 5$ for aged *Crtc2* AKO mice). **b**, An insulin tolerance test (ITT) was performed on mice. Blood glucose levels at the designated time points are shown (left). The area under the curve was calculated for the insulin tolerance test for each mouse (right). Data represent mean ± s.d. ($n = 7$ for young *Crtc2* f/f mice; $n = 8$ for aged *Crtc2* f/f mice; and $n = 7$ for aged *Crtc2* AKO mice). **c**,**d**, Body weight (**c**) and body composition analysis (**d**) on young *Crtc2* f/f mice ($n = 5$), aged *Crtc2* f/f mice ($n = 9$) and aged *Crtc2* AKO mice ($n = 9$) are shown. Data represent mean ± s.e.m. **e**, A representative image showing the effect of aging and adipocyte-specific depletion of *Crtc2* on organ size. **f**, The effect of aging and adipocyte-specific depletion of *Crtc2* on the organ weight of liver, VAT, SAT and BAT. Data represent mean ± s.e.m. ($n = 5$ for young *Crtc2* f/f mice; $n = 4$ for aged *Crtc2* f/f mice; and $n = 4$ for aged *Crtc2* AKO mice). **g**, A representative image showing hematoxylin-eosin staining of liver and adipose tissues from young *Crtc2* f/f mice, aged *Crtc2* f/f mice and aged *Crtc2* AKO mice. A representative image is shown (scale bars, 100 μm). **h**, Effects of aging and *Crtc2* depletion on SAT:VAT ratio. Data represent mean ± s.e.m. ($n = 6$ for young *Crtc2* f/f mice; $n = 3$ for young *Crtc2* AKO mice; $n = 6$ for aged *Crtc2* f/f mice; and $n = 5$ for aged *Crtc2* AKO mice). *P* values were determined using one-way analysis of variance (ANOVA) with Tukey's multiple comparisons test (**a**–**d**,**f**,**h**).

https://doi.org/10.1038/s43587-023-00460-8

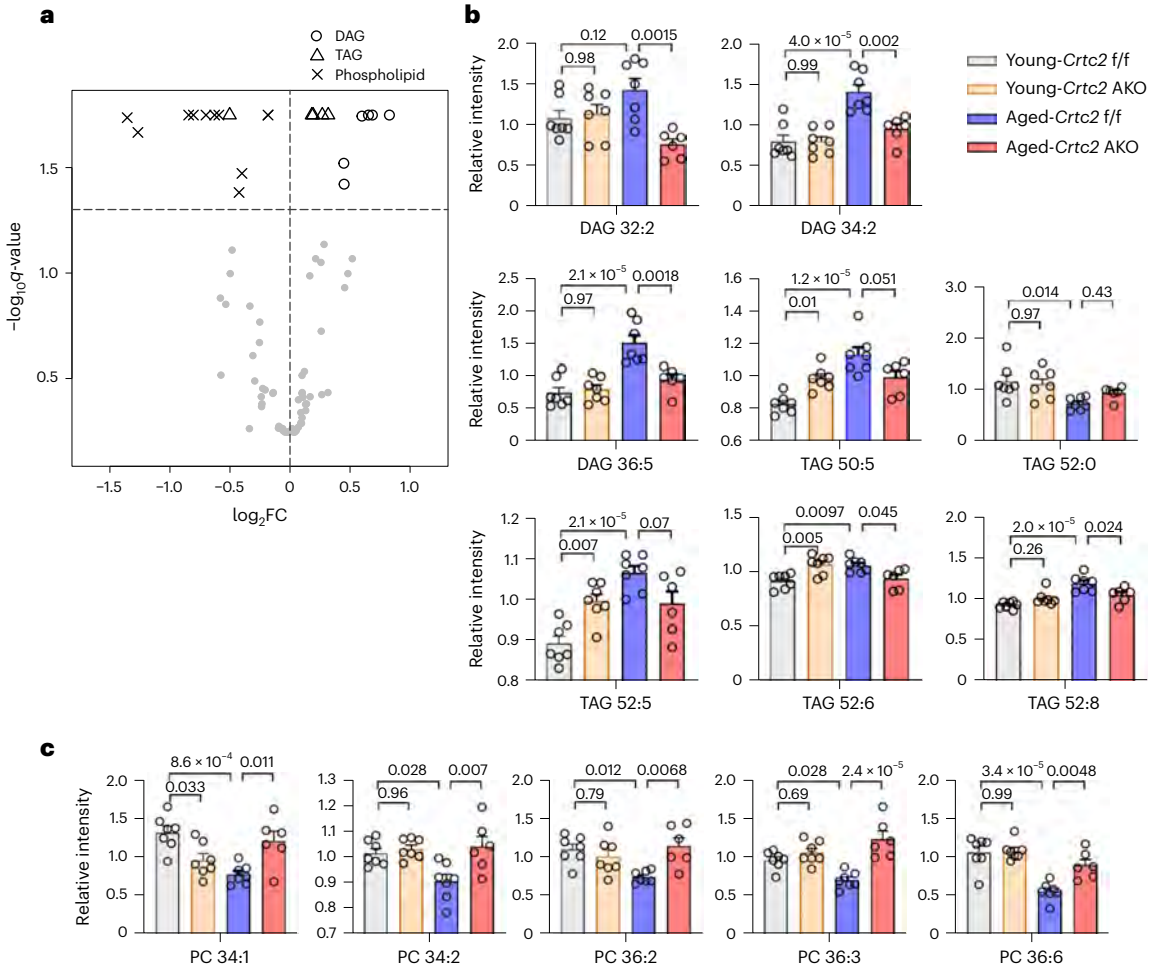

Fig. 2 | CRTC2 is linked to the age-associated changes in lipid profiling of VAT. Lipid profiling analysis was performed using male young *Crtc2* f/f mice (3 months old), young *Crtc2* AKO mice (3-month-old), aged *Crtc2* f/f mice (18 months old) and aged *Crtc2* AKO mice (18 months old). **a**, Volcano plot of lipid metabolites from lipid-profiling analysis of mouse VAT in vivo. Fold change was defined as a square root of multiplication of mean fold change (aged control versus young control) and the inverse of mean fold change (aged AKO versus aged control). *q* values were estimated based on permuted *P* values. **b**, Quantification of DAGs and TAGs, common forms of glycerides, from mouse VAT in vivo. Only metabolites with the lowest *q* value from the permutation analysis are shown. **c**, Quantification of PC, a common form of phospholipids, from mouse VAT in vivo. Only metabolites with the lowest *q* value from the permutation analysis are shown. Data in **b** and **c** represent mean ± s.e.m. ($n = 7$ for young *Crtc2* f/f mice; $n = 7$ for young *Crtc2* AKO mice; $n = 7$ for aged *Crtc2* f/f mice and $n = 6$ for aged *Crtc2* AKO mice). *P* values were determined using one-way ANOVA with Tukey's multiple comparisons test (**b**,**c**).

pronounced as peaks between young WT mice and aged WT mice did not overlap and, at least in the first principal component, peaks from aged *Crtc2* AKO mice were moving toward those from young control mice (Supplementary Fig. 3a). In accordance with the histological analysis of liver (Supplementary Fig. 1f), the PCA showed no differences in hepatic lipid profiles between young WT mice and young *Crtc2* AKO mice (Supplementary Fig. 3b). In general, we observed a dramatic increase in most classes of hepatic lipids in aged WT mice compared to the younger counterparts (Supplementary Fig. 3c). Of note, we observed a specific decrease in a subset of lipids, including cholesterol esters, diacylglycerols (DAGs) and TAGs in the livers of *Crtc2* AKO mice compared to aged WT mice (Supplementary Fig. 3c). We did not observe noticeable changes in hepatic lipids between young WT mice and young *Crtc2* AKO mice (Supplementary Fig. 3d). While we observed only a modest change in hepatic expression of genes responsible for lipogenesis (for example *SREBP1c*, *SCD1* and *FAS*) in response to aging or by *Crtc2* AKO, we found a specific increase in hepatic expression of genes responsible for fatty acid uptake or lipid droplet formation (such as *CD36*, *Cidec*, *FABP4* and *PPARγ2*) by aging, which was reduced upon adipocyte-specific depletion of *Crtc2* (Supplementary Fig. 3e). We did not observe changes in expression of genes involved in fatty acid β-oxidation by aging in both genotypes (Supplementary Fig. 3f). These data suggest that age-dependent accumulation of hepatic lipids is largely due to the increased potential for fatty acid uptake, presumably by the dysregulation of lipid metabolism in adipose tissues and is corrected by adipocyte-specific deletion of *Crtc2* in VAT.

Similar to our hepatic lipid remodeling, recovery patterns of lipid species in VAT also seem to be attributed to *Crtc2* AKO. We performed permutation tests to detect statistically significant up–down or down–up changes, recapturing the species' level by *Crtc2* AKO (Extended Data Fig. 3a). As was the case for liver, age-induced increase in TAG and DAG levels came close to that of young controls in aged *Crtc2* AKO mice (Fig. 2a,b and Extended Data Fig. 3a). On the other hand, a large number of phospholipids, especially phosphatidylcholine (PC), in VAT were decreased in aged control mice compared to young control mice and adipocyte-specific depletion of *Crtc2* restored it to levels seen in young controls (Fig. 2c and Extended Data Fig. 3a). Notably, a recent report suggested that accelerated PC turnover is responsible for the inflammation of adipose tissues in obesity[25], hinting that aging could similarly perturb PC homeostasis in VAT. Additionally, we observed lipid

metabolism rewiring in *Crtc2* KO primary adipocytes from VAT. The m+5 fractional labeling of citrate derived from [U-^{13}C] glutamine was reduced in *Crtc2* KO adipocytes compared to that in controls (Extended Data Fig. 3b). The labeled carbons in citrate m+5 were from the reductive glutamine flux, one of the major carbon sources of lipid synthesis[26].

These data suggest that age-dependent changes in lipid composition in liver and VAT were partially prevented by adipocyte-specific depletion of *Crtc2*, indicating that age-dependent changes in systemic lipid metabolism could be controlled by CRTC2-mediated signaling pathway in VAT.

BCAA is associated with elevated CRTC2–Hes-1 axis in VAT

We then turned our attention to the metabolomics analysis of VAT. Metabolites with recovery patterns were detected based on permutation analysis and their residing pathways were explored to find metabolic signatures. The pathways with more than two hits were: BCAA metabolism, cysteine and methionine metabolism, citrate cycle, nucleotide sugar metabolism, purine metabolism and pyrimidine metabolism (Extended Data Fig. 4). Furthermore, we color-coded metabolic pathways using RNA sequencing (RNA-seq) data and metabolomics data to visually inspect metabolic signatures from integrated data (Fig. 3a). We found the concordant changes in RNA expression and the concentration of metabolites in BCAA catabolism. Expression of genes encoding enzymes for BCAA catabolism was generally reduced in VAT of aged WT mice compared to their young counterparts in RNA-seq analysis (Extended Data Fig. 5a–e), which was confirmed by qPCR (Fig. 3b). At the protein level, both BCKDHB and BCAT2 but not BCKDHA were reduced in VAT by aging (Extended Data Fig. 6a). Expression of BCAA catabolic genes and proteins were recovered upon depletion of *Crtc2* both in VAT and differentiated adipocytes (Fig. 3b and Extended Data Fig. 6a,b). We observed a specific decrease in BCAA catabolites in VAT of aged WT mice compared to their young counterparts, which was restored in VAT of aged *Crtc2* AKO mice from global metabolomic profile analysis (Fig. 3c and Extended Data Fig. 4). In particular, the hydroxy-methyl-butyrate (HMB) level was reduced by aging, which was restored by adipocyte-specific depletion of *Crtc2* in VAT. The 3-hydroxy-3-methylglutaric acid (3-HMG) level also tended to be reduced by aging and was also elevated in VAT of aged *Crtc2* AKO mice in comparison to aged WT mice (Fig. 3d). The levels of BCAA catabolites in VAT were not different between WT and *Crtc2* AKO mice of a young age (Extended Data Fig. 4). These data suggested that age-dependent reduction of BCAA catabolism was restored in *Crtc2*-depleted VAT, via the regulation of the BCKDH complex and BCAT2. Isotope-tracing experiments confirmed the increased leucine catabolic flux toward downstream metabolites in the *Crtc2* AKO model. When primary adipocytes were fed with [U-^{13}C] leucine, five carbons in HMB and 3-HMG were ^{13}C labeled (Fig. 3e). As intracellular concentration of 3-HMG in adipocyte was lower than the analytical limit, we quantified isotopomer distribution of HMB via targeted metabolite analysis. The amount of five-carbon-labeled HMB was significantly increased in both differentiated adipocytes and pre-adipocytes from *Crtc2* AKO mice after a 4-day culture (Fig. 3f). Moreover, we observed an increase in secreted extracellular five-carbon-labeled HMB in both differentiated adipocytes and pre-adipocytes from *Crtc2* AKO mice (Fig. 3g). Conversely, plasma BCAA levels were elevated in aged WT mice compared to young controls, which were significantly reduced in aged *Crtc2* AKO mice (Fig. 3h). This finding is notable as the increased plasma level of BCAA has been shown to be closely associated with insulin resistance and type 2 diabetes not only in rodents but also in humans[27–30]. Furthermore, a strong negative correlation was reported between the expression levels of BCAA metabolic genes in mouse adipose tissue with fasting insulin levels and IR (HOMA-IR)[31]. Of note, recent studies have shown that increased BCAAs in the diet also reduced lifespan in rodents[32,33], suggesting that plasma BCAA levels could be positively associated with aging or age-associated metabolic disorders. Therefore, increased systemic BCAA levels could be attributed to BCAA dysmetabolism, especially in adipose tissues[34,35].

To explore a potential mechanism for the increased gene expression associated with BCAA catabolism in *Crtc2*-depleted VAT, we measured the relative expression of two transcription factors that were shown to control BCAA catabolism. Kruppel-like factor 15 (KLF15) is a known master regulator for glucose and amino acid metabolism, including BCAA[36]. While we observed that KLF15 expression was reduced in response to aging in VAT, no specific changes in KLF15 expression were detected upon adipocyte-specific depletion of *Crtc2* in VAT, showing that KLF15 might not be involved in the changes in gene expression responsible for BCAA catabolism by CRTC2 (Fig. 3b). On the other hand, expression of PPARγ, a major regulator of adipogenesis and amino acid catabolism[37], was significantly reduced in VAT from aged WT mice compared to their younger counterparts, which was restored by adipocyte-specific depletion of *Crtc2* (Fig. 3b). Previous studies revealed that CREB was shown to down-regulate expression of PPARγ in the liver by transcriptional activation of HES1, a transcriptional inhibitor for PPARγ[38]. As CRTC2 functions as a coactivator for CREB, we suspected that *Hes1* expression could be altered in response to aging or depletion of *Crtc2* in VAT. Indeed, we were able to show that *Hes1* expression was elevated by aging and was reduced by adipocyte-specific depletion of *Crtc2* in VAT (Fig. 3b), corroborating our hypothesis that the elevated CRTC2–HES1 axis and the resultant downregulation of PPARγ could be responsible for the BCAA dysmetabolism in VAT in aged mice compared to their younger counterparts (Supplementary Fig. 4a). Indeed, knockdown of *Hes1* in differentiated adipocytes led to the increased expression of PPARγ and BCAA catabolic enzymes such as BCKDHA and BCKDHB, corroborating our hypothesis that regulation of *Hes1* expression was crucial in the control of BCAA catabolism (Supplementary Fig. 4b).

Fig. 3 | CRTC2–Hes-1 axis is critical in age-associated increase in plasma BCAA levels. RNA-seq and metabolomics analysis were performed using male young *Crtc2* f/f mice (3 months old), young *Crtc2* AKO mice (3 months old), aged *Crtc2* f/f mice (18 months old) and aged *Crtc2* AKO mice (18 months old). **a**, Schematic diagram showing the flow of RNA-seq (top). Volcano plot of FPKM from RNA-seq ($n = 3$ mice per group, bottom). The 45 genes annotated to mmu00280, BCAA degradation, in the KEGG pathway are colored in red. The fold change was calculated as square root of multiplication of fold change between aged controls versus young controls and the inverse of fold change between aged AKO and aged controls. *q* values were estimated based on *P* values from the permutation analysis to quantify the extremeness of observed recovery patterns. *P* value from the chi-squared test for independence (d.f. of 1) between significant genes with *q* value with <0.05 and BCAA pathway; *P* value from the same test between genes with decreasing fold change and BCAA pathway was <0.0001. FPKM, fragments per kilobase of transcript per million mapped reads. **b**, qPCR analysis on genes in BCAA catabolism in mature adipocytes ($n = 4$ mice per group). **c**, Volcano plot of aqueous metabolites from metabolic profiling analysis of VAT ($n = 7$ young *Crtc2* f/f mice; $n = 6$ aged *Crtc2* f/f mice; and $n = 6$ aged *Crtc2* AKO mice). Fold change is defined as the square root of multiplication of mean fold change (aged controls versus young controls) and the inverse of mean fold change (aged AKO versus aged controls). *q* values were estimated based on *P* values from the permutation analysis. **d**, Quantification of HMB and 3-HMG from VAT ($n = 7$ young *Crtc2* f/f mice; $n = 6$ aged *Crtc2* f/f mice; and $n = 5$ aged *Crtc2* AKO mice). **e**, Schematic illustration of the transformation of leucine carbon to intermediates in BCAA catabolism. **f**,**g**, Quantification of intracellular (**f**) or extracellular (**g**) HMB isotopomer distribution from [^{6}-U-^{13}C] leucine labeling of differentiated adipocytes (left) and pre-adipocytes (right) ($n = 3$ biological replicates per group). **h**, Plasma BCAA concentration mice ($n = 7$ young *Crtc2* f/f mice; $n = 3$ young *Crtc2* AKO mice; $n = 8$ aged *Crtc2* f/f mice; and $n = 6$ aged *Crtc2* AKO mice). Data represent mean ± s.e.m. *P* values were determined using one-way ANOVA with Dunnet's multiple comparison test (**b**) or Tukey's multiple comparisons test (**d**,**f**–**h**).

https://doi.org/10.1038/s43587-023-00460-8

Crtc2 AKO mice displays reduced mTORC1-mediated senescence

Age-associated decline in the metabolic function is instigated by cellular senescence. Indeed, we were able to observe an increased expression of markers for the cellular senescence (p16, p19 and p21) in the VAT of aged WT mice compared to the younger controls (Fig. 4a). In compliance with improved metabolic phenotypes, expression of senescence marker genes was dramatically reduced in VAT of aged *Crtc2* AKO mice compared to the aged control mice, suggesting that the age-initiated senescence in VAT was delayed with adipocyte-specific depletion of *Crtc2*. In line with this result, we found that cellular senescence was less pronounced in *Crtc2*-depleted VAT compared to the controls in aged mice, but not in young mice, as evidenced by the measurement of SA-β galactosidase as well as the immunohistochemical assessment and western blot analysis of γ-H2AX and p21 levels (Fig. 4b–d and Supplementary Fig. 5a,b).

Recent studies revealed that the age-stimulated decrease in SIRT1/AMPK pathway and the reciprocal increase in mTORC1 pathway could be causal to the cellular senescence as well as various metabolic disorders[39–43]. Previously, we have shown that depletion of *Crtc2* in liver

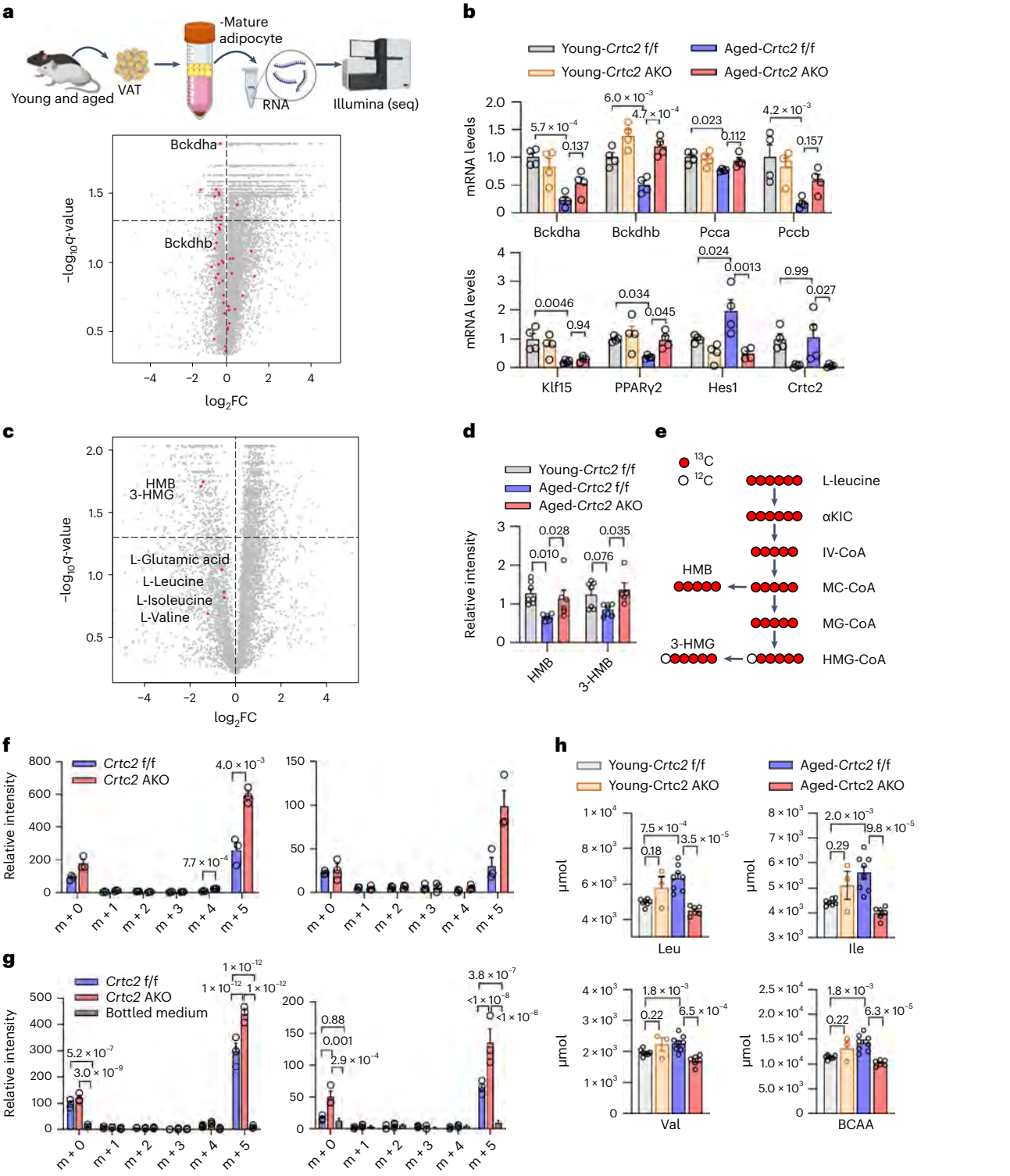

https://doi.org/10.1038/s43587-023-00460-8

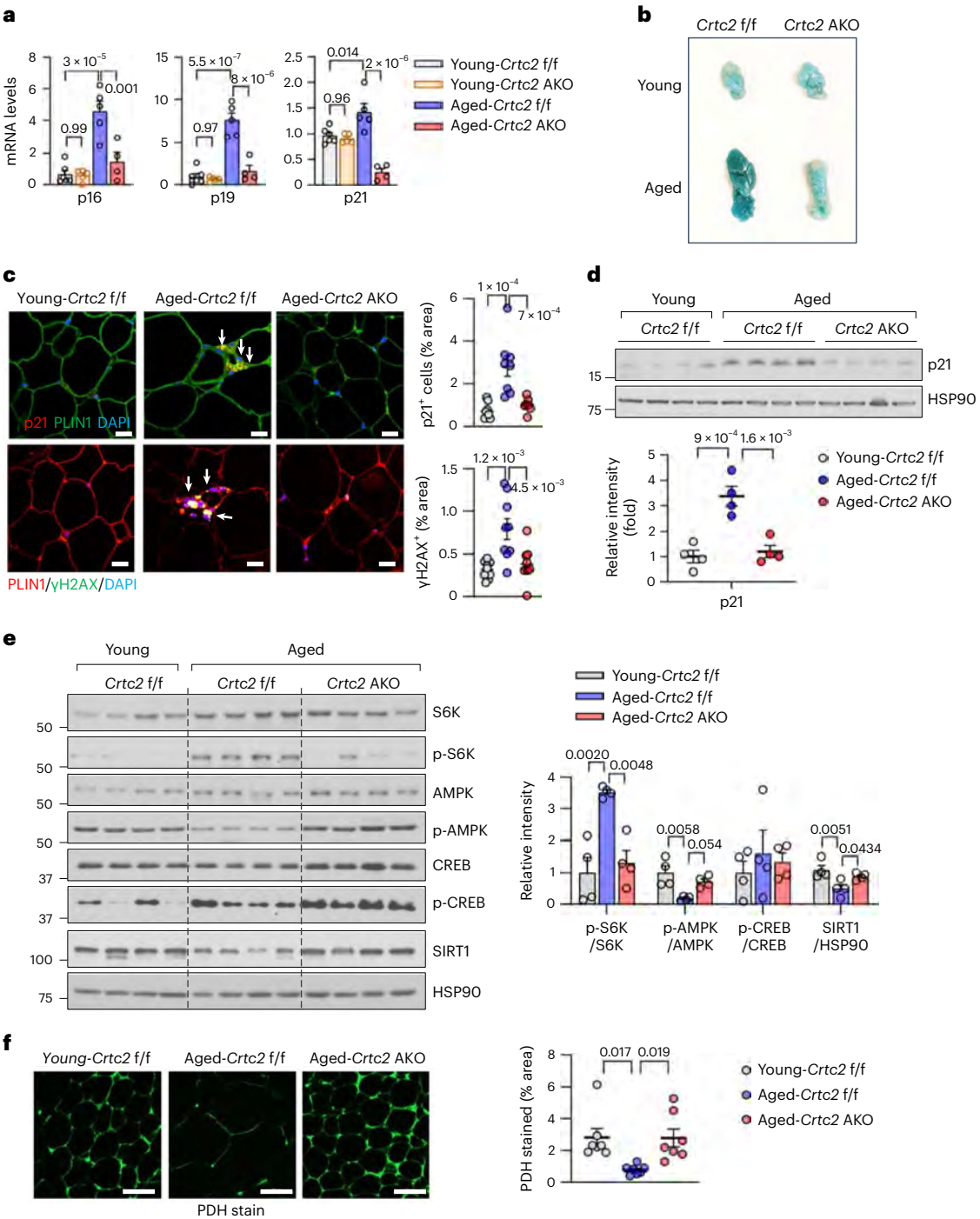

Fig. 4 | Adipocyte-specific *Crtc2* knockout reduced cellular senescence in adipose tissues. a, qPCR analysis of senescence-associated genes in VAT of mice. Data represent mean ± s.e.m. ($n = 6$ for young *Crtc2* f/f mice (3 months old); $n = 5$ for young *Crtc2* AKO mice (3 months old); $n = 5$ for aged *Crtc2* f/f mice (18 months old); and $n = 4$ for aged *Crtc2* AKO mice (18 months old)). **b**, Representative SA-β-gal staining to detect cellular senescence of VAT from young *Crtc2* f/f mice (3 months old), young *Crtc2* AKO mice (3 months old), aged *Crtc2* f/f mice (21 months old) and aged *Crtc2* AKO mice (21 months old). **c**, Representative immunohistochemical staining showing effects of aging and adipocyte-specific depletion of *Crtc2* on cellular senescence in VAT of young *Crtc2* f/f mice (3 months old), aged *Crtc2* f/f mice (19 months old) and aged *Crtc2* AKO mice (19 months old) (scale bars, 20 μm). Quantitation of p21 and γH2AX are also shown. Data represent mean ± s.e.m. ($n = 8$ biological replicates per group for p21 and $n = 9$ biological replicates per group for γH2AX). DAPI,4,6-diamidino-2-phenylindole. **d**, A representative western blot analysis showing effects of aging and adipocyte-specific depletion of *Crtc2* on proteins involved in senescence from VAT of young *Crtc2* f/f mice (3 months old), aged *Crtc2* f/f mice (18 months old) and aged *Crtc2* AKO mice (18 months old). Quantitation of p21 bands was also shown. Data represent mean ± s.e.m. ($n = 4$ biological replicates per group). **e**, A representative western blot analysis showing effects of aging and adipocyte-specific depletion of *Crtc2* on proteins involved in senescence, AMPK pathway and mTORC1 signaling in VAT of young *Crtc2* f/f mice (3 months old), aged *Crtc2* f/f mice (18 months old) and aged *Crtc2* AKO mice (18 months old). Relative values for p-S6K/S6K, p-AMPK/AMPK, p-CREB/CREB and SIRT1/HSP90 are shown. Data represent mean ± s.e.m. ($n = 4$ biological replicates per group). **f**, A representative PDH staining showing effects of aging and adipocyte-specific depletion of *Crtc2* on mitochondria in VAT of young *Crtc2* f/f mice (3 months old), aged *Crtc2* f/f mice (19 months old) and aged *Crtc2* AKO mice (19 months old) (scale bars, 50 μm). Percentage of PDH stained area is also shown. Data represent mean ± s.e.m. ($n = 7$ biological replicates per group). PDH, pyruvate dehydrogenase. *P* values were determined using one-way ANOVA with Tukey's multiple comparisons test (**a**,**c**–**f**).

led to the decreased expression of miR-34a, a known inhibitor of SIRT1, resulting in the increased fatty acid β-oxidation as well as plasma FGF21 levels[16]. We found that miR-34a, miR-146b and miR-132 were significantly induced in response to aging in mature adipocytes from VAT (Supplementary Fig. 5c), each of which has been previously shown to target SIRT1 (refs. 44–46). Among the three miRNAs, miR-34a and miR-132 were demonstrated to be transcriptionally controlled by CREB and/or CRTC2, suggesting that age-dependent regulation of these miRNAs might be mediated by the CREB/CRTC2 pathway[16,47]. Notably, expression of miR-34a, but not of miR-132, was significantly downregulated by adipocyte-specific depletion of *Crtc2* in mature adipocytes from VAT of aged mice (Supplementary Fig. 5c), demonstrating that age-associated increase in miR-34a might affect SIRT1-dependent signaling in a CRTC2-dependent manner. Indeed, expression of SIRT1 was significantly decreased in VAT from aged WT mice compared to their younger counterparts (Fig. 4e). In addition, p-AMPK levels were similarly altered in response to aging. Previous report suggested that BCAA, especially leucine, can enhance mTORC1 pathway, thus inhibiting insulin signaling pathway[48]. In line with age-associated changes in the BCAA catabolic pathway, we were able to observe an increase in mTORC1 pathway in response to aging, as evidenced by the increased p-S6K1 levels in aged WT mice compared to the controls (Fig. 4e). Of note, adipocyte-specific depletion of *Crtc2* dramatically reverted age-mediated changes in cellular signaling, as shown by the restoration of the SIRT1/AMPK pathway and the inhibition of the mTORC1 pathway in VAT compared to WT counterparts (Fig. 4e and Supplementary Fig. 6a). Restoration of cellular signaling was also pronounced in aged *Crtc2*-depleted SAT but only mildly shown in BAT, further supporting our hypothesis that the function of CRTC2 is more pronounced in WAT than in BAT (Supplementary Figs. 6b,c and 7).

To verify further the importance of CRTC2 in mTORC1-mediated cellular senescence, we differentiated AP cells from *Crtc2* f/f mice and *Crtc2* AKO mice in vitro in the presence of senescence-inducing agents, with or without mTORC1 inhibitor rapamycin. As was the case in vivo, *Crtc2* depletion showed reduced p-S6K1 levels and cellular senescence as shown by p21 levels and SA-β-gal staining in differentiated adipocytes, underscoring the importance of the CRTC2–mTORC1 axis in cellular senescence (Supplementary Fig. 8). Rapamycin treatment effectively blunted senescence-inducing-agent-associated increases in cellular senescence and this effect was further enhanced in *Crtc2*-deficient adipocytes, likely due to the elimination of the residual mTORC1 activity that may have been partially active upon *Crtc2* depletion.

The balance between AMPK signaling and the mTORC1 pathway is closely associated with the maintenance of mitochondrial function[49]. As expected, functional mitochondrial contents were reduced in response to aging in VAT, as shown by immunohistochemical staining of pyruvate dehydrogenase (Fig. 4f). Adipocyte-specific depletion of *Crtc2* partially restored the age-associated decline in functional mitochondria in VAT. No specific differences in mitochondria from VAT of young WT mice and young *Crtc2* AKO mice (Supplementary Fig. 9) were seen. These data suggest that adipocyte-specific depletion of *Crtc2* protects adipose tissues from age-associated decline in mitochondria, in part by a reciprocal modulation of the AMPK–mTORC1 axis.

Crtc2 promotes age-induced remodeling of adipose tissues

To gain a better insight into how the VAT microenvironment evolves during aging and by adipocyte-specific depletion of *Crtc2*, we performed scRNA-seq on stromal vascular fractions (SVFs) derived from the VAT of *Crtc2* f/f or AKO mice at two different age groups, young (5 months old) and aged (18 months old). We profiled a total of 55,656 cells passing our quality control (QC) criteria, sampled from two biological replicates for each condition, with an average of 2,985 genes and 10,320 unique molecular identifiers (UMIs) per cell (Supplementary Fig. 10a). To characterize the age-dependent dynamics of cellular composition within VAT, we applied a graph-based clustering algorithm and annotated each cell cluster based on the expression of cell-type marker genes, resulting in a single-cell atlas of 18 cell types derived from 27 cell clusters (Fig. 5a and Supplementary Fig. 10b,c). The cell types were organized into three broad groups of cells: lymphoid, myeloid and nonimmune cells. The cell-type composition analysis accounting for batch effects revealed that all groups were globally reorganized during aging and the age-dependent changes of lymphoid and nonimmune cells were restored by *Crtc2* AKO in aged mice (Fig. 5b and Supplementary Fig. 10d–f).

The lymphoid cells were further subdivided into 14 cell types by re-clustering lymphoid cells and annotating each cluster based on lymphoid cell markers (Supplementary Fig. 11a–c). We observed a previously identified age-related expansion of $CD3^+$ T cells, $CD19^+$ B cells and a reduction of innate immune cells[50,51] and many of these age-associated changes were partially rescued by adipocyte-specific depletion of *Crtc2* (Supplementary Fig. 11d–h). In the B-cell subsets, memory B cells were expanded in aged WT mice and reduced in aged *Crtc2* AKO mice, in line with a previous report showing the age-related and NLRP3 inflammasome-dependent expansion of memory-like B cells, termed as aged adipose B cells (AABs), in fat-associated lymphoid clusters of VAT[52]. The age-associated expansion of various T-cell subsets, including $CD4^+$ T (T.Naive.CD4 and T.Conv.CD4), $CD8^+$ T (T.Naive.CD8 and T.Cytotoxic.CD8) and regulatory T (T_{reg}) cells, has been well described in VAT[50,53]. Consistent with previous reports, they were increased in aged WT mice and adipocyte-specific depletion of *Crtc2* partially restored their aberrant increase (Supplementary Fig. 11d–h). The selective depletion of VAT-resident T_{reg} cells in aged mice is known to prevent age-associated insulin resistance[53], suggesting that VAT-resident T_{reg} cells are important for the observed phenotype of aged *Crtc2* AKO mice. Notably, we observed that adaptive and innate immune responses in T-cell subsets were activated in aged WT mice, which was partially rescued by adipocyte-specific depletion of *Crtc2* in T.Conv.CD4, T_{reg} and T.Cytotoxic.CD8 cells (Supplementary Fig. 11i). Together, these results suggest that the perturbed immune responses in the VAT upon aging may contribute to age-associated metabolic disorders and that perturbed responses can be partially rescued by adipocyte-specific depletion of *Crtc2*.

Fig. 5 | Age-associated decline in adipogenic potential of VAT is restored by *Crtc2* deficiency. scRNA-seq analysis was performed using male young *Crtc2* f/f mice (5 months old), young *Crtc2* AKO mice (5 months old), aged *Crtc2* f/f mice (18 months old) and aged *Crtc2* AKO mice (18 months old). **a**, Uniform Manifold Approximation and Projection (UMAP) plot of 55,656 cells across four conditions ($n = 2$ biological replicates per group). Each color indicates annotated cell types. DC, dendritic cell; NK, natural killer. **b**, Bar-plot showing proportion of annotated cell types for each condition. **c**, *t*-distributed stochastic neighbor embedding (*t*-SNE) plots of AP cells showing schematic representation of trajectories (top) and violin plots of marker expression of *Dpp4* and *Fabp4* (bottom). **d**, Heat map showing scaled gene expression trends along differentiation trajectories. **e**, *t*-SNE plots of AP cells. Cells are highlighted by each condition (top), colored by pseudotime or branch probabilities of each path (bottom). **f**, Box-plot representing branch probabilities of 15,609 AP2 cells across different paths and conditions with two independent biological replicates. The first quartile, median and third quartile are shown with whiskers lengthened 1.5 × interquartile range (IQR). **g**, Adipocyte progenitor cells ($PDGFR\alpha^+$) isolated from VAT of young *Crtc2* f/f mice (3 months old), young *Crtc2* AKO mice (3 months old), aged *Crtc2* f/f mice (20 months old) and aged *Crtc2* AKO mice (20 months old) were analyzed. Cell proliferation was assessed every 2 d after plating using the CyQuant assay (left). Data represent mean ± s.e.m. ($n = 3$ biological replicates per group). For adipocyte differentiation, cells were incubated with insulin and rosiglitazone for 6 d and then stained with LipidTOX (right, scale bars, 150 μm)). Representative data are shown. *P* values were determined using a Student's *t*-test (**f**,**g**).

https://doi.org/10.1038/s43587-023-00460-8

Given the reduction of the myeloid compartment during aging, we next sought to characterize the cellular heterogeneity of adipose tissue macrophages (ATMs) that have primary roles in controlling metabolic homeostasis and inflammatory state in VAT. We identified two distinct subsets of ATMs, Mac.Lyve1 and Mac.Cd9, distinguished by the differential expression of *Lyve1*, *Cd9* and *Trem2* (Supplementary Fig. 12a–c). The Mac.Lyve1 subset showed higher expression of *Lyve1*, *Cd38* and *Cd209f* (Supplementary Fig. 12b), sharing a signature of

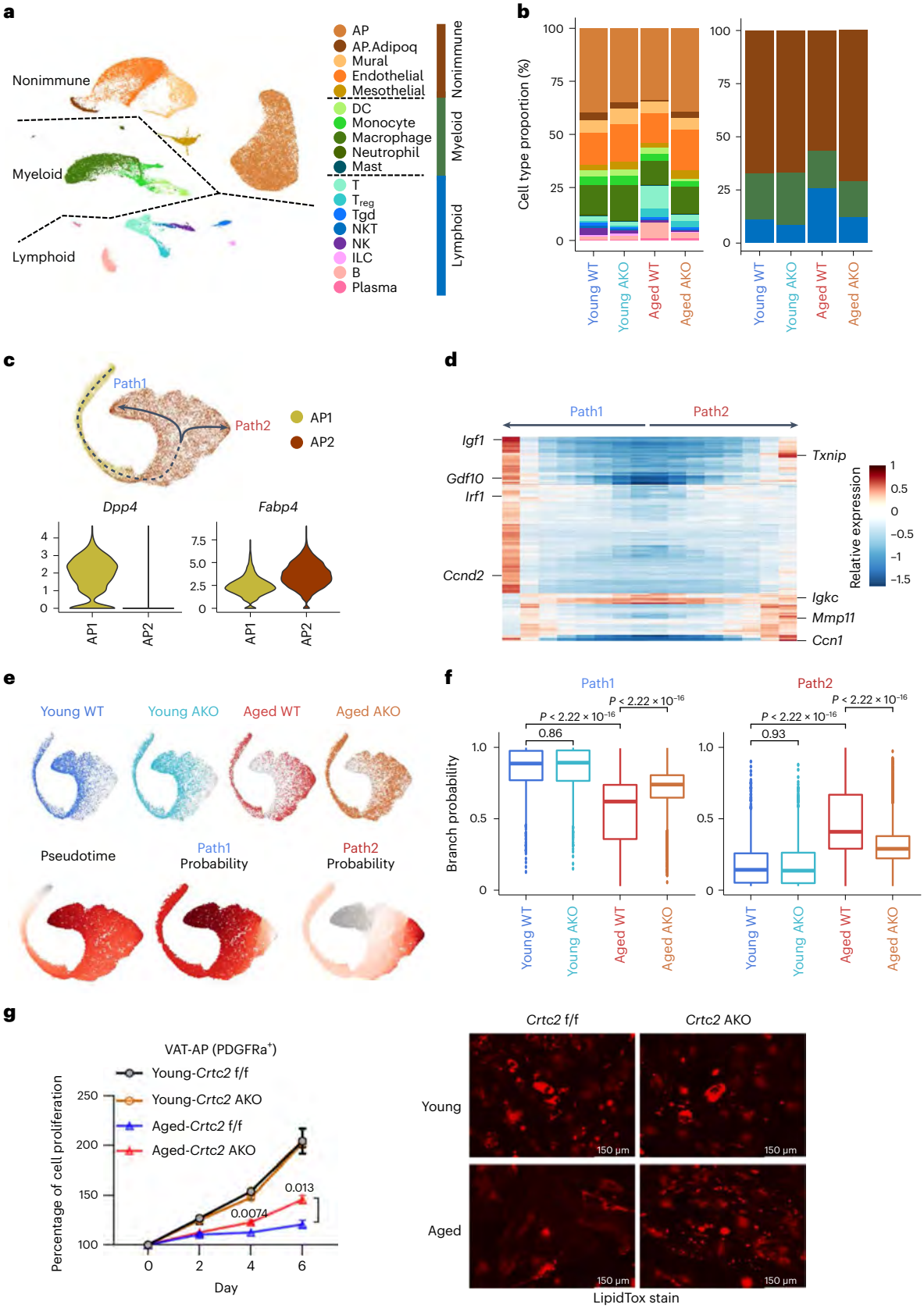

https://doi.org/10.1038/s43587-023-00460-8

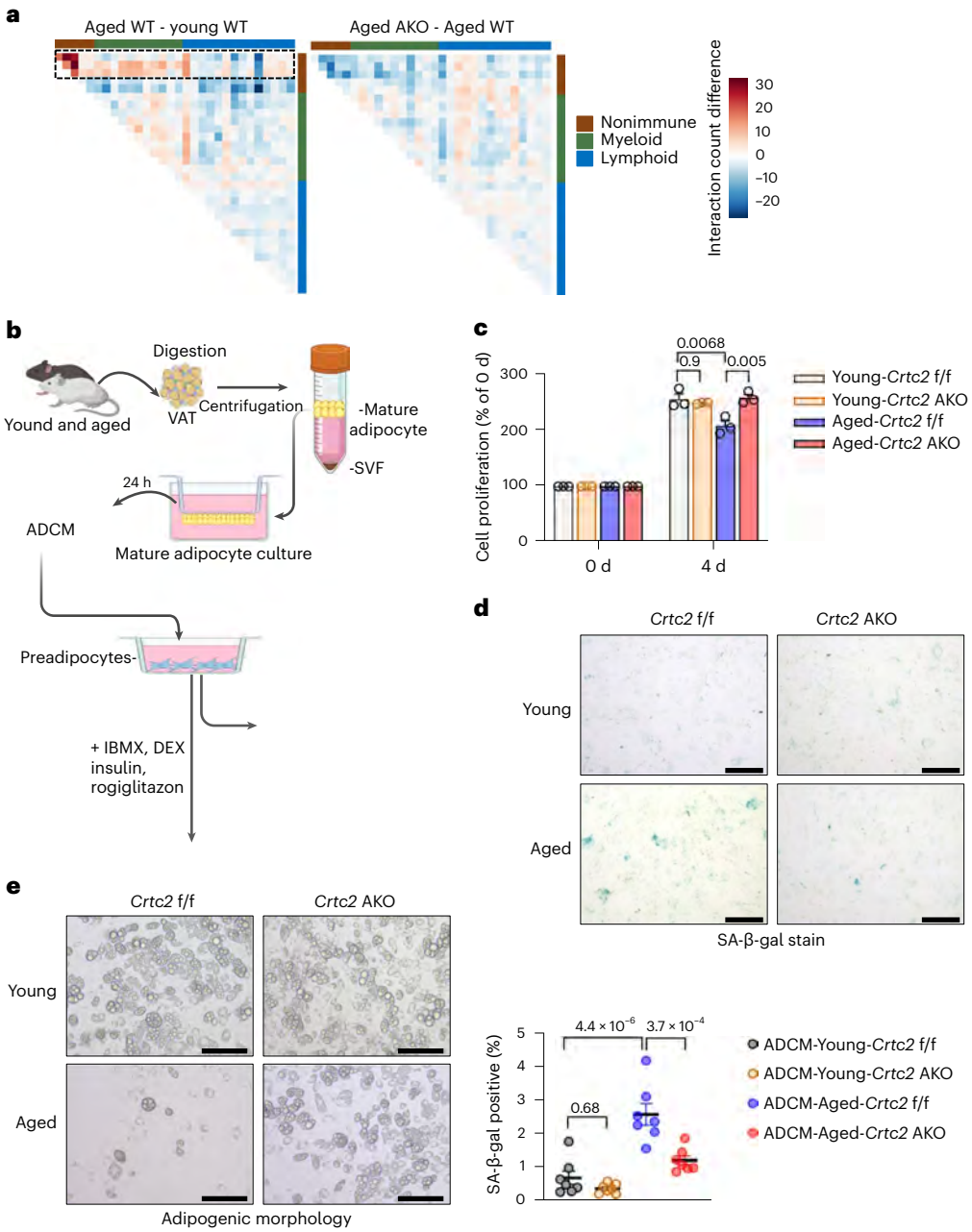

Fig. 6 | CRTC2-dependent regulation of secretome is critical in age-associated remodeling of VAT. a, Heat map showing the differences of the number of ligand–receptor interactions between the aged *Crtc2* f/f and young *Crtc2* f/f mice (left) or between aged *Crtc2* AKO and aged *Crtc2* f/f mice (right) as in Fig. 5. Areas showing the most dramatic reversed effect are highlighted. **b**, Experimental scheme showing the preparation of ADCM using mature adipocytes from VAT of young *Crtc2* f/f mice (3 months old), *Crtc2* AKO mice (3 months old), aged *Crtc2* f/f mice (18 months old) and aged *Crtc2* AKO mice (18 months old) (top, left). **c**, Effects of ADCM on cell proliferation of AP cells (top, right). Data represent mean ± s.e.m. ($n = 3$ biological replicates per group). **d**, Effects of ADCM on cellular senescence. A representative image with SA-β-gal staining is shown (top, scale bars, 250 μm). Data in bar graph represent mean ± s.e.m. ($n = 7$ biological replicates per group, bottom). **e**, Effects of ADCM on adipogenic differentiation of AP cells are also shown (scale bars, 150 μm). Representative data are shown. *P* values were determined using one-way ANOVA with Tukey's multiple comparisons test (**c**,**d**).

recently identified Lyve1^{hi}MHCII^{lo} perivascular macrophages (Supplementary Fig. 12j)[54]. The diet-induced obesity induces a reduction of the Mac.Lyve1 subset[55], which promotes inflammatory cell infiltration and tissue fibrosis[54]. In contrast, the Mac.Cd9 subset was characterized by the increased expression of *Cd9*, *Cd63*, *Trem2*, *Cx3cr1* and MHC-II-encoding genes (Supplementary Fig. 12b), sharing common genes of recently described CD9^{+}, Lyve1^{lo}MHCII^{hi} and Trem2^{+} lipid-associated ATMs (Supplementary Fig. 12j)[54–56]. These ATM subsets are expanded during obesity, contributing to obesity progression by metabolizing neuronally released norepinephrine or adapting to obesity by preventing adipocyte hypertrophy[55–57]. The Mac.Cd9 subset was expanded during aging and reduced in aged *Crtc2* AKO mice, whereas the Mac.Lyve1 subset showed the opposite age-dependent changes (Supplementary Fig. 12d–i). These data indicate that *Crtc2* in adipocytes is a critical regulator for the response of ATMs during aging and highlight its importance for the age-dependent change of the ratio of Mac.Cd9 to Mac.Lyve1 macrophages that is associated with inflammation and fibrosis in VAT. Furthermore, we found that adipocyte-specific depletion of *Crtc2*

https://doi.org/10.1038/s43587-023-00460-8

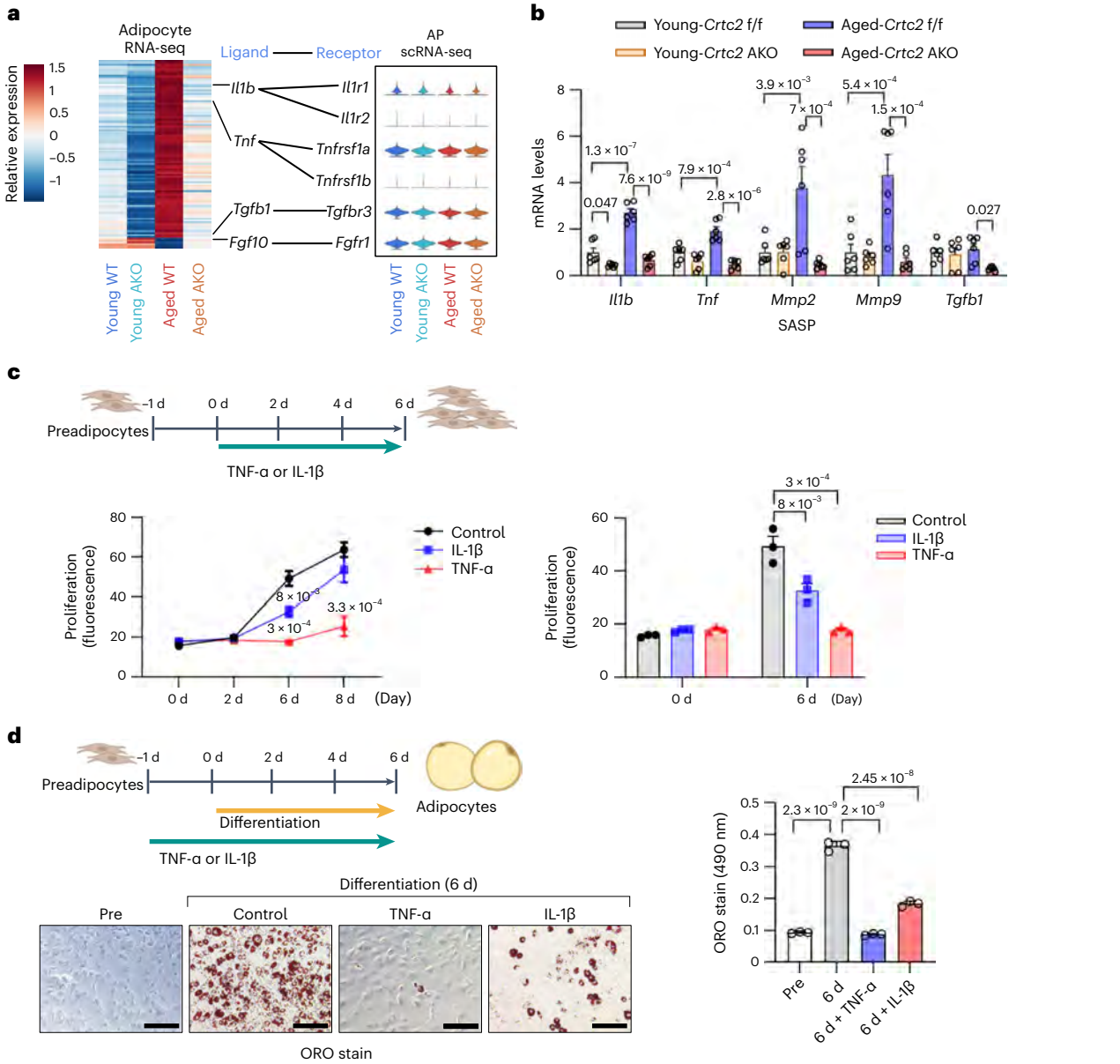

Fig. 7 | Effects of SASP factors on cellular senescence and adipogenic potential of AP cells. a, Heat map showing the relative expression of differentially expressed genes encoding ligands across all conditions (left) and violin plots showing the normalized expression of the corresponding receptor genes for each condition (right) as in Fig. 5. **b**, qPCR analysis of genes encoding SASP in mature adipocytes from VAT of young *Crtc2* f/f mice (3 months old), young *Crtc2* AKO mice (3 months old), aged *Crtc2* f/f mice (18 months old) and aged *Crtc2* AKO mice (18 months old). Data represent mean ± s.e.m. ($n = 6$ mice per group). **c**,**d**, Adipocyte progenitor cells (PDGFRα$^+$) isolated from VAT of young *Crtc2* f/f mice were used to analyze the effect of SASPs. Cell proliferation was assessed every 2 d after plating using the CyQuant assay (**c**). Data represent mean ± s.e.m. ($n = 3$ biological replicates per group). For adipocyte differentiation, cells were incubated with insulin and rosiglitazone for 6 d and then stained with Oil Red O (ORO) staining (**d**, scale bars, 150 µm). Representative data are shown. Data represent mean ± s.d. (n = 3 biological replicates per group). *P* values were determined using one-way ANOVA with Tukey's multiple comparisons test (**b**–**d**).

protected VAT from age-induced fibrosis, as shown by Picro Sirius Red (PSR) staining and qPCR analysis of genes responsible for fibrosis and extracellular matrix (ECM) remodeling, including *Col1a1*, *Col6a1*, *Mmp2* and *Ctsl* (Extended Data Fig. 7a,b). Notably, we observed a specific increase in macrophage infiltration and expression of proinflammatory cytokine genes (*Mcp1* and *Il1b*) in livers of aged WT mice compared to their younger counterparts and adipocyte-specific depletion of *Crtc2* reversed this age-associated phenomenon (Supplementary Fig. 13a,b). In addition, we observed that adipocyte-specific depletion of *Crtc2* specifically protected livers from age-induced fibrosis, as shown by PSR staining and qPCR analysis of genes responsible for fibrosis, including *Acta2* (α-SMA), *Mmp12*, *Timp1* and *Col1a1* (Supplementary Fig. 13c,d). These results collectively suggest that adipocyte-specific depletion of *Crtc2* protected mice from developing age-induced fibrosis not only in VAT but also in the peripheral tissues such as the liver.

Crtc2 deficiency restores adipogenic potential in aged mice

To determine whether the adipogenic potential of APs can be affected by adipocyte-specific depletion of *Crtc2* in aged mice, we analyzed differentiation trajectories of APs using Palantir (Fig. 5c–f). As APs are known to be composed of distinct subpopulations with different adipogenic potential[58,59], we divided APs into two subsets: multipotent

https://doi.org/10.1038/s43587-023-00460-8

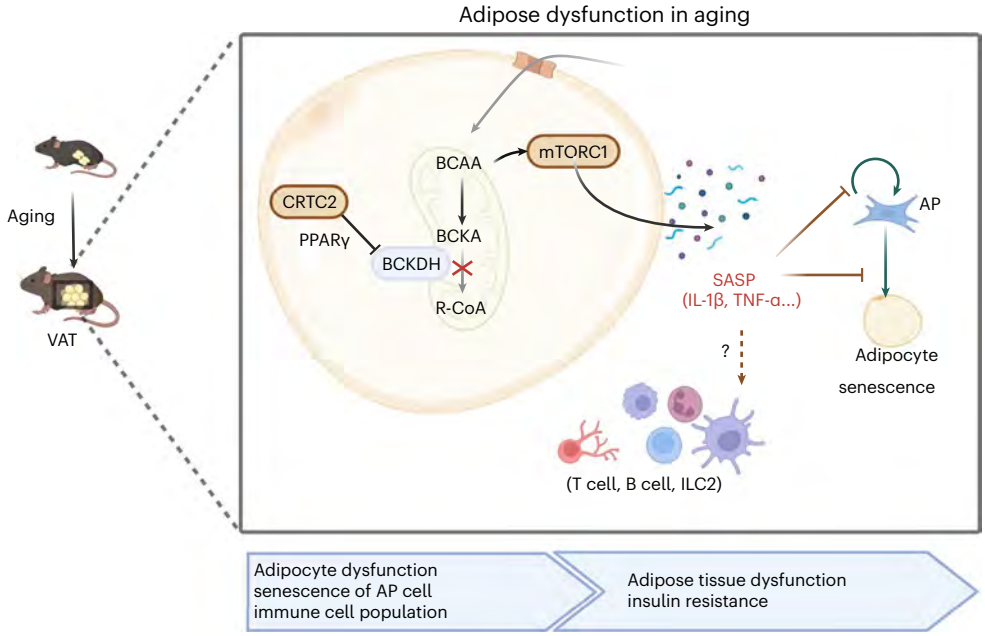

Fig. 8 | A proposed model showing the role of CRTC2 in age-associated remodeling of VAT. CRTC2 expression in adipocytes is elevated upon aging, leading to the reduced BCAA catabolism and AMPK signaling. This in turn promotes activation of mTORC1 pathway, leading to the enhancement of cellular senescence in mature adipocytes. Elevated secretion of SASP factors TNF-α and IL-1β deteriorates the normal function of AP cells, resulting in the reduced adipogenic potential and metabolic dysfunction of VAT upon aging.

AP1-expressing *Dpp4* and committed AP2-expressing preadipocyte markers such as *Icam1* and *Fabp4* (Fig. 5c and Extended Data Fig. 8a). The two AP subsets were also distinguished by enhanced activity of PI3K, WNT and TGF-β signaling pathways in AP1 (Extended Data Fig. 8b). Notably, the activity of TGF-β, WNT and hypoxia-signaling pathways, playing an important role in fibrosis and inflammation in adipose tissues[60–62], was enhanced in AP2 cells of aged WT mice compared to young WT mice but diminished by adipocyte-specific depletion of *Crtc2* (Extended Data Fig. 8b). Trajectory analysis revealed that APs have two trajectories differentiating toward the adipogenic (Path1) or fibro-inflammatory terminal state (Path2) (Fig. 5c–e). The terminal state of Path1 highly expressed *Igf1*, *Gdf10*, *Irf1* and *Ccnd2*, signatures associated with adipogenesis and proliferation[63–65]. In contrast, the terminal state of Path2 was characterized by the expression of *Mmp11* and *Ccn1*, which are associated with fibrosis and inflammation[66,67] (Fig. 5d). Notably, cells from aged WT mice were more likely to differentiate along Path2 compared to younger mice, which was partially rescued by adipocyte-specific depletion of *Crtc2* in aged mice (Fig. 5e,f). Indeed, we found that AP cells from aged *Crtc2*-depleted VAT showed an increased proliferation compared to those from aged WT mice (Fig. 5g). Furthermore, AP cells from aged *Crtc2*-depleted VAT showed reduced cellular senescence and an increased potential for adipogenesis compared to aged WT controls (Fig. 5g and Extended Data Fig. 8c), showing indeed that the age-dependent decline in adipogenic potential is prevented by adipocyte-specific depletion of *Crtc2*. These data further support our hypothesis that age-induced changes in mature adipocytes could induce an environment that promotes senescence and reduces the adipogenic potential of AP cells and adipocyte-specific depletion of *Crtc2* could prevent the age-associated decline of adipose tissue function in mice.

Next, we sought to determine how adipocyte-specific depletion of *Crtc2* remodels the adipose tissue microenvironment in aged mice. We hypothesized that ligands that were differentially expressed upon aging or the depletion of *Crtc2*, could affect components of adipose tissue microenvironment by ligand–receptor interactions. Cellular crosstalk analysis showed that most of age-associated cellular interactions occurred between APs and other components, which were partially rescued by adipocyte-specific depletion of *Crtc2* (Fig. 6a). We suspected that secretion of specific molecules from mature adipocytes might be involved in the remodeling of adipose tissue microenvironment, especially of AP cells, in response to aging. To verify this hypothesis, we obtained mature adipocytes from VAT of young WT mice, young *Crtc2* AKO mice, aged WT mice or aged *Crtc2* AKO mice and incubated them in the tissue culture medium to isolate the adipocyte conditioned medium (ADCM) (Fig. 6b). As expected, treatment of AP cells with ADCM from aged WT mice led to the reduced proliferation rate compared to cells treated with ADCM from young WT mice or young *Crtc2* AKO mice. Of note, AP cells treated with ADCM from aged *Crtc2* AKO mice showed similar proliferation rate in comparison to AP cells treated with ADCM from young mice (Fig. 6c). Furthermore, we found that AP cells treated with ADCM from aged WT mice showed an increased incidence of senescence and a reduced adipogenic potential compared with AP cells treated with ADCM from young WT mice (Fig. 6d,e). AP cells treated with ADCM from aged *Crtc2* AKO mice showed a similar adipogenic potential in comparison to AP cells treated with ADCM from young mice, suggesting that depletion of *Crtc2* in mature adipocytes led to the reduced production of specific secretory molecules that promote age-induced changes in AP cells.

From adipocyte RNA-seq analysis, we identified 103 differentially expressed genes encoding ligands between young and aged mice (adjusted $P < 0.05$), showing the reversal of age-dependent expression changes by *Crtc2* AKO (Fig. 7a). Of 103 ligand genes, 97 genes upregulated in aged adipocytes, including *Tgfb1*, *Il1b* and *Tnf*, were associated with fibrosis and inflammation. The corresponding receptors were expressed in APs. In contrast, six ligand genes downregulated in aged adipocytes included *Fgf10*, which is known to promote adipogenesis[68], whose receptors were mainly expressed in APs (Fig. 7a). Among the identified potential ligands, we confirmed that a subset of genes encoding SASP factors were elevated in aged mature adipocytes, including *Il1b* (encoding interleukin (IL)-1β) and *Tnf* (encoding tumor necrosis factor (TNF)-α), but not *Tgfb*, by qPCR (Fig. 7b). Notably, *Il1b* and *Tnf* are downstream targets of mTORC1 (ref. 69), which was shown to be

enhanced upon aging in VAT (Fig. 4e). Of note, expression of these SASP factors were significantly reduced in *Crtc2*-depleted aged mature adipocytes, suggesting that they might be responsible for the changes in AP cells in vivo. Indeed, in cultured adipocyte model, we were able to observe an increased expression of SASP factors in response to senescence-inducing agents, such as bleomycin or H_2O_2. Again, *Crtc2*-knockout adipocytes were not only resistant to cellular senescence in response to senescence-inducing agents, but also showed reduced expression of SASP factors (Extended Data Fig. 9a–d), confirming our hypothesis that genetic depletion of *Crtc2* reduced expression of SASP factors in adipocytes.

Next, we wanted to determine whether these SASP factors are responsible for the changes in the property of AP cells. Knockdown of IL-1R (IL-1β receptor) or TNFR1 (TNF-α receptor) reduced the inhibitory effect of aged ADCM on cellular proliferation in AP cells (Extended Data Fig. 10a). Also, aged ADCM-mediated enhancement of cellular senescence was also partially inhibited upon depletion of IL-1R or TNFR1 in AP cells (Extended Data Fig. 10b). Similarly, the inhibitory effect of ADCM from senescent adipocytes on adipocyte differentiation was partially blocked by treatment of anti-IL-1β or anti-TNF-α (Extended Data Fig. 9e). Furthermore, we found that the treatment of IL-1β or TNF-α reduced the proliferation of AP cells and adipogenic potential (Fig. 7c,d), further supporting our hypothesis that these SASP factors could be causal to the changes in the adipogenic potential of AP cells and the decline of the functional adipose tissues upon aging.

Discussion

Age-associated decline in cellular function results in chronic disorders by compromising systemic metabolic homeostasis. As WAT plays a central role in maintaining whole-body metabolism by functioning as a center for nutrient storage and distribution and a key endocrine organ by secreting adipokines[4], dysfunction of WAT upon aging could be one of the major culprits for age-associated metabolic disorders. Age-mediated deterioration of functional WAT could result in dyslipidemia and chronic systemic inflammation, among other symptoms, leading to ectopic lipid accumulation, inflammation and insulin resistance in peripheral tissues[2,5]. Indeed, dietary or genetic intervention targeting adipose tissues could extend the healthspan at least in the model organism, suggesting that recovering functional WAT, especially VAT, could be beneficial in preventing age-associated metabolic disorders in mammals, including humans. Indeed, we observed that adipocyte-specific depletion of *Crtc2* prevented mice from developing age-associated metabolic disorders, confirming a specific role of adipose tissues in age-associated progression of metabolic diseases.

VAT is composed of multiple cell types, including mature adipocytes, AP cells, as well as various immune cells, including macrophages, T cells and neutrophils[2] and age-induced remodeling of VAT promotes changes in the composition and the property of these cells. Adipocyte size is increased by aging, which is associated with the enhanced infiltration of proinflammatory macrophages around the dead-like adipocytes, presumably due to augmented senescence, leading to an elevated inflammatory state. In addition, an age-induced increase in visceral adiposity also results in the accumulation of certain classes of lymphoid cells such as T_{reg} cells and memory B cells, leading to age-associated metabolic disorders[52,53]. In the present study, we found that depletion of *Crtc2* in mature adipocytes led to the specific decrease in age-induced changes in immune cells, suggesting that expression of certain chemokines that were crucial for the enrichment of these immune cells was altered upon depletion of *Crtc2* in mature adipocytes. Indeed, we observed that several chemokines from the large CC chemokine family and CXC family, known to enhance recruitment of specific immune cells[70], were downregulated upon *Crtc2* depletion (Supplementary Fig. 14). Of note, a recent report showed that some of these chemokines such as CXCL1, CXCL2 and CCL2 are indeed transcriptional targets of adipose CRTCs, which are crucial in macrophage infiltration in VAT under obesity[71]. Further study is necessary to delineate the relationship between age- and CRTC2-dependent regulation of these chemokines in mature adipocytes and the resultant recruitment of immune cells in VAT.

In addition to these changes, the potential for the replenishment of mature adipocytes with the newly synthesized adipocytes is also impaired in aged individuals, presumably due to the diminished adipogenic potential and/or numbers of AP cells. In line with this result, we showed that functional AP cells were reduced in aged VAT compared to that in younger counterparts (Fig. 5f). Furthermore, we observed reduced adipogenic potential of AP cells from aged VAT compared to that in younger controls, showing indeed that aging diminished the adipogenic potential of AP cells (Fig. 5g). These data are in line with previous reports, which underscored the critical role of senescence of AP cells in age-dependent decline in functional adipose tissues[9,72]. We reasoned that SASP factors such as TNF-α and IL-1β from mature adipocytes promote the cellular senescence of AP cells, leading to the expression of a second array of SASP factors, including activin A from senescent AP cells, which in turn accelerates the cellular senescence of AP cells and adjacent cell types in a paracrine manner, as described in a previous study[9]. Indeed, we also found that AP cells from aged mice secrete higher levels of activin A compared to younger controls, which was significantly reduced in AP cells from *Crtc2* AKO mice (Supplementary Fig. 15). Notably, we showed that adipocyte-specific depletion of *Crtc2* prevented age-induced reduction of adipogenic potential and induction of cellular senescence, showing the importance of functional mature adipocytes in preservation of healthy adipose tissues by limiting secretion of SASP factors.

Circulating BCAA levels are often associated with insulin resistance and type 2 diabetes in humans[73]. Indeed, recent studies suggested that increased BCAAs might be causal to the promotion of metabolic disorders. A couple of mechanisms have been postulated to explain the role of BCAAs (or their metabolites) in affecting metabolic pathways. Although still debatable, persistent activation of mTORC1 signaling by BCAAs could be the direct cause for systemic insulin resistance[28,29,74–76]. Alternatively, elevated BCAA levels in the bloodstream by BCAA dysmetabolism could cause metabolic disorders. In support of this model, expression of key proteins in BCAA catabolism, such as the BCAT and BCKDH complex E1-α, is markedly reduced in adipose tissues of obese rodents as well as humans, leading to elevated circulating BCAA levels and its immediate catabolite, BCKA[34,35]. As the catabolism of BCAA mainly occurs in mitochondria, accumulation of incomplete BCAA catabolites could result in mitochondrial dysfunction. In addition, obesity could initially promote mitochondrial dysfunction, leading to the deterioration of the machinery for BCAA catabolism. In our study, we identified that circulating BCAA levels were elevated in response to aging, due to the reduction of BCAA catabolism in VAT. The defects of BCAA catabolism by aging also coincided with age-induced reduction in functional mitochondria in aged VAT compared to that in their younger counterparts. Notably, we showed that adipocyte-specific depletion of *Crtc2* reverted the age-induced increase in circulating BCAA levels, via the restoration of the expression of genes encoding BCAA catabolism in VAT.

Further work is needed to address the limitations of the present study. First, we analyzed only male mice in this study, thus requiring additional analysis in female mice to elucidate whether the elevated CRTC2–BCAA axis by aging is present in a non-sex-specific manner. Furthermore, addition of more time points between young and aged groups or even at older ages would be useful to track the changes in cellular signaling, metabolomics and gene expression profiles in response to aging and genetic deficiency of *Crtc2* throughout the lifespan. Finally, it is desirable to compare the relevance of the current findings in humans in the future.

In summary, we found that adipocyte-specific depletion of *Crtc2* prevented mice from developing age-associated metabolic disorders

by mainly affecting the architecture of VAT. Specifically, depletion of *Crtc2* reduced age-associated decline in functional mature adipocytes, leading to the preservation of anti-inflammatory macrophages and healthy AP cells by reducing the secretion of SASP factors, in part by blocking age-induced BCAA dysmetabolism (Fig. 8). Our study illustrates the importance of adipose tissues in the progression of age-associated systemic metabolic disorders and suggests that adipocyte-specific inhibition of *Crtc2* activity or restoration of BCAA catabolic potential could be beneficial in relieving age-associated anomalies in mammals.

Methods

Animals

All animal experiments were carried out under approved protocols by the Korea University Institutional Animal Care and Use committee (KUIACUC-2018-0031). Mice had free access to food (chow diet, 1314 IRR, Altromin) and water and were caged at 22 °C with 12-h light–dark cycles and 50% humidity. For the generation of adipocyte-specific *Crtc2* KO (*Crtc2* AKO) mice, *Crtc2* floxed mice[16] were crossed with adiponectin-Cre transgenic mice.

For the metabolic studies, young (3–5 months old) and aged (18–21 months old) male mice with C57BL/6N background were used. For the glucose tolerance test, mice were fasted for 16 h and then injected intraperitoneally with glucose (1.5 g kg^{-1} body weight). For the insulin tolerance test, 6-h-fasted mice were intraperitoneally injected with insulin (1 U kg^{-1} body weight). Blood glucose was measured with an automatic glucose monitor (One Touch, LifeScan). For insulin signaling, either PBS or insulin (0.2 U per mouse) was injected intraperitoneally and liver and adipose tissues were collected for further analyses.

Fat mass and lean mass were measured by an NMR analyzer Bruker Minispec LF50 (Bruker Optics) and indirect calorimetry was assessed by an indirect calorimetric chamber (TSE phenoMaster, TSE systems) at the Korea Mouse Phenotyping Center (Seoul National University).

Western blot analysis

Western blot analysis was performed using 20–90 µg whole lysates that were prepared in RIPA buffer (25 mM Tris, pH 7.4, 150 mM NaCl, 1% Triton X-100, 1% sodium deoxycholate, 0.1% SDS, 1 mM EDTA, 5% glycerol, 50 mM NaF, 5 mM β-glycerophosphate and 1 mM phenylmethyl sulfonyl fluoride) with a cocktail of protease inhibitors (GenDEPOT).

Chemicals and antibodies

Chemicals and antibodies used in this work are summarized in Supplementary Table 1.

Isolation of mature adipocytes and SVF

Adipose tissues were digested in F10-HAM medium (Gibco) containing 1.5% BSA (GenDEPOT) and 0.1% collagenase type I (Worthington) at 37 °C for 30 min and were filtered through a 300-µm cell strainer[77]. After centrifugation at 4 °C, 500*g* for 7 min, floating mature adipocytes were collected for further analysis. For SVF isolation, pellets were filtered through a 70-µm cell strainer, centrifuged at 4 °C, 500*g* for 7 min and then were collected as SVF.

Cell culture

For the preparation of AP cells, VAT was minced and digested with 1 mg ml^{-1} collagenase (type I) at 37 °C for 30 min. The reaction was stopped with DMEM (Hyclone) containing 10% fetal bovine serum (FBS) (Hyclone) and the resultant lysates were filtered through 70-µm filters, centrifuged at 500*g* for 7 min and washed with the same buffer. AP cells were then isolated using the phycoerythrin (PE)-anti-mouse CD140a antibody and anti-PE Microbeads (Miltenyi) according to the manufacture's protocol. AP cells were expanded in DMEM with 10% FBS. For differentiation experiments, cells were washed and the medium was supplemented with differentiation induction cocktail (2 µM dexamethasone, 0.5 mM IBMX, 0.5 µM rosiglitazone, 1.5 nM T_3, 125 µM indomethacin and 5 µg ml^{-1} insulin) for 2 d. Afterwards, cells were switched to the maintenance medium (DMEM, 5 µg ml^{-1} insulin and 0.5 µM rosiglitazone) every 2 d.

RNA preparation, qRT–PCR, RNA-seq and miRNA quantification

Total RNA was isolated using Trisure (Bioline) and RNeasy kit (QIAGEN) according to the manufacturer's protocols. Complementary DNA was synthesized using Goscript Reverse transcription system (Promega) according to the manufacture's protocol. Quantitative PCR with reverse transcription (qRT–PCR) was performed in triplicate using a SensiFAST SYBR green mix (Bioline) and CFX connect real-time system with Bio-Rad CFX Manager v.3.0 (Bio-Rad). The messenger RNA levels were normalized to ribosomal L32. mRNA sequencing was performed by Macrogen as described[77].

For miRNA quantification, total RNA was isolated using a miRNeasy mini kit (QIAGEN). Total RNA was reverse transcribed using a miScript II RT kit (QIAGEN). Primers specific for mouse miRNAs were purchased from QIAGEN. The values were normalized to RNU6B.

Histological analysis

Adipose tissues and liver were isolated from mice and were fixed with 10% formalin (Sigma). Histological changes were examined by hematoxylin and eosin staining. For immunostaining, paraffin-embedded tissues were deparaffinized in xylene and were subsequently rehydrated using ethanol and water. For antigen retrieval, slides were submerged in 10 mM sodium citrate buffer (pH 6.0) and heated for 20 min. Slides were incubated with 3% H_2O_2 and blocked with 1% BSA solution for 1 h, followed by incubation with specific primary antibodies at 4 °C overnight. Signals were detected with anti-rabbit IgG HRP and DAB substrate kit (Vector). Slides were counterstained with Harris hematoxylin (Sigma) and observed with a Leica DMi8 light microscope with Leica Application suite X (3.7.0.20979) (Leica) or LSM 700/800 laser scanning microscopy with ZEN v.2.1 system (Cal Zeiss). The collagen deposition was assessed by a PSR stain kit (Abcam) according to the manufacturer's protocol.

Cell proliferation assay

Following seeding in 96-well plate, the medium was aspirated and cells were incubated with the dye binding solution from the CyQuant NF Cell Proliferation Assay kit (Invitrogen) according to the manufacturer's protocol. Fluorescence was measured in a microplate reader Synergy HT with BioTek Synergy HT Gen5 v.2.01 (BioTek).

Adipose tissue extraction

To extract metabolites and lipid species in VAT, previously used methods were modified and adopted[78]. Then, 20 mg frozen tissue was weighed and placed in extraction solution (600 µl methanol:chloroform at 66:33 (v/v)) and homogenized at 2,823*g* for 20 s twice. Homogenized samples were further sonicated for 15 min and 200 µl chloroform and water were separately added. After 1 min of vortexing, extracts were stored at 4 °C for 10 min, followed by centrifugation at 4 °C, 18,213*g* for 20 min. Upper aqueous supernatant and lower lipophilic solution were separately transferred to clean microcentrifuge tubes and dried using a speed vac evaporator and nitrogen evaporator, respectively. Powdered samples were stored at −80 °C till LC–MS analysis. On the same day as LC–MS analysis, dried polar metabolites were immediately re-dissolved in water:acetonitrile at 25:75 solution for polar metabolite metabolomics. Similarly, dried lipid spices were re-dissolved in isopropanol:acetonitrile at 10:90 (v/v) for lipidomics.

Global lipidomic profiling based on LC–MS

LC-ESI–MS/MS analysis for both lipidomics and metabolomics was performed on a triple TOF 5600 MS/MS System (AB Sciex) combined

with a UPLC system (Waters). Lipid species were analyzed in the range m/z 50–1,500. The following specific settings were used: ion spray voltage, 5,500 V; source temperature, 500 °C; nebulizer gas pressure, 60 psi; drying gas pressure, 60 psi; and curtain gas pressure, 30 psi. LC separations were carried out on an Acquity UPLC BEH C18 column (Waters). Column temperature and flow rate were set to 35 °C and 0.35 ml min^{-1}, respectively. The mobile phase A was 10 mM ammonium acetate in acetonitrile:water at 40:60 (v/v) and the mobile phase B was 10 mM ammonium acetate in acetonitrile:isopropanol at 10:90 (v/v). The gradient elution started at 60% A:40% B and B was increased linearly to 65% at 5 min, 70% at 12 min and 99% at 15 min. Then, 1% A:99% B was kept for 2 min and column was equilibrated for 3 min. Pooled QC samples were also measured to check data. For each sample, 5 µl were injected with a partial loop mode for positive and negative ionization polarity modes separately from auto-samplers at 4 °C.

Global metabolomic profiling based on LC–MS

For metabolomics, the analyzed mass range was m/z 50–1,000. The following specific settings were used: ion spray voltage, 4,500 V; source temperature, 500 °C; nebulizer gas pressure, 60 psi; drying gas pressure, 60 psi; and curtain gas pressure, 30 psi. Merck SeQuant ZIC HILIC column (Merck) was used for separation and the temperature was set to 35 °C. The flow rate was 0.4 ml min^{-1}. Mobile phase A and B consisted of acetonitrile:10 mM ammonium acetate in water:formic acid at 90:10:0.1 (v/v/v) and acetonitrile:10 mM ammonium acetate in water/formic acid at 50:50:0.1 (v/v/v), respectively. The gradient elution started at 99% A:1% B, held for 2 min and B was increased linearly to 45% at 8 min and 99% at 9 min. Then, 1% A:99% B was kept for 2 min and the column was equilibrated for 4 min at the end of each run. Samples were randomly ordered for the analysis and pooled QC samples were injected several times between 5 µl sample injection, with a partial loop mode for positive and negative ionization polarity modes, kept separately from the vial on the auto-sampler at 4 °C.

MS spectral data processing

The spectral data were processed by MarkerView (v.1.3.1; AB Sciex) software to find peaks, to perform the alignment and to generate peak tables made of m/z and retention times. Then, the data were normalized based on total ion count of each sample. To select reproducible peaks, stepwise quality control process was performed as follows: whether coefficient of variation of relative ion intensity of features from QC sample injections is <20; whether the feature is considered as an isotope of other features; and whether the VIP score from PLSDA is >1 and simultaneously, the *P* value from a Student's *t*-test is <0.1 for either young control versus aged control or aged control versus aged *Crtc2* AKO mice.

Molecular annotation

MS/MS patterns from features were tentatively identified by comparing the experimental data to the METLIN (metlin.scripps.edu) database. Especially for lipidomic features, automated annotation was performed through the annotation pipeline in MS-DIAL (v.3.90), followed by a manual confirmation procedure.

Serum extraction

Mouse serum was frozen at −80 °C immediately after the centrifugation of blood samples. Then, 20 µl each thawed samples were separately mixed with 220 µl 2:1 (v/v) chloroform:methanol solution at −20 °C for lipid metabolite extraction followed by vortexing for 1 min. Then, 40 µl water was added for aqueous metabolite extraction followed by vortexing for 1 min. Samples were rested at 4 °C for 10 min followed by centrifugation, at 30,130*g* for 20 min. Upper aqueous supernatant was transferred to clean microcentrifuge tubes and dried using nitrogen evaporator. Powdered samples were stored at −80 °C. On the same day as LC–MS analysis, dried polar metabolites from upper aqueous phase were immediately re-dissolved in water:acetonitrile 1:1 (v/v) solution for the analysis.

Targeted metabolomics based on LC–MS

Liquid chromatography–mass spectrometry based targeted metabolite analysis was performed on an Agilent 1290 Infinity LC and an Agilent 6490 Triple Quadrupole (TQ) MS system equipped with Agilent Jet Stream ESI source (Agilent Technologies). Samples were analyzed in multiple reaction monitoring mode.

To quantify the level of BCAA catabolites, LC separations were carried out on Kinetex C18 column (100 × 2.1 mm, particle size 1.7 µm, Phenomenex) on reverse phase mode for 12 min. Column temperature and flow rate were set to 30 °C and 0.45 ml min^{-1}, respectively. The binary gradient system consisted of 0.1% formic acid in water (solvent A) and acetonitrile (solvent B). The linear gradient used for elution and equilibrating the initial gradient for subsequent runs was 1–10% B from 0–3 min, 10–25% B from 3–5 min, 25–40% B from 5–6 min, 40% B from 6–7 min, 40–1% B from 7–8 min and 1% B from 8–12 min. The column effluent was introduced into a TQ mass detector operating in negative ESI mode.

To quantify the level of BCAA in mouse serum extracts, LC separations were carried out on an Intrada Amino Acid column (50 × 3 mm, particle size 3 µm, Imtakt) for 13 min. Column temperature and flow rate were set to 35 °C and 0.6 ml min^{-1}, respectively. The binary gradient system consisted of 50 mM ammonium formate in water (solvent A) and acetonitrile with 0.1% formic acid (solvent B). The linear gradient used for elution and equilibrating the initial gradient for subsequent runs was 14% A from 0–3 min, 14–100% A from 3–10 min, 100–14% A from 10–12 min and 14% A from 12–13 min. The column effluent was introduced into a TQ mass detector operating in positive ESI mode. The MassHunter Workstation (v.B.06.00; Agilent Technologies) was used for data acquisition and analysis.

Isotope tracing for BCAA catabolism

Isotopic labeling was performed by feeding cells with DMEM without L-leucine (Welgene) supplemented with 0.8 mM [U-13C]-L-leucine (Cambridge Isotope Laboratories), 10% FBS (Thermo Fisher Scientific) and 1% penicillin–streptomycin (Gibco) for 4 d. To extract intracellular metabolite, cells were washed with ice-cold PBS twice and metabolites were quenched in liquid nitrogen. Then frozen cells were extracted with 240 µl 50:30:20 (v/v/v) methanol:acetonitrile:water solution per each well (six-well plates) at −20 °C. For the extraction of metabolites from the culture medium, 100 µl medium was mixed with 500 µl methanol at −20 °C. All extracted metabolites were stored at −80 °C for 1 h, followed by centrifugation twice at 30,130*g* for 20 min.

Quantification and statistical analyses

To capture the overall trend in our multiomics data, descriptive statistical analysis and PCA was conducted in R (v.4.2.1). The magnitude of recovery patterns was defined as a square root of multiplication of mean fold change (aged control versus young control) and the inverse of mean fold change (aged AKO versus aged control). Group labeling of metabolic abundances or FPKM values was permuted to calculate how often more extreme recovery patterns are observed. The *q* values were estimated based on the permuted *P* value[79].

For Gene Ontology (GO) analysis, genes with *q* values <0.05 were considered significant genes. By using a set of significant genes, hypergeometric tests were conducted to find significantly enriched pathways in the GO database using goseq R package (v.1.52.0)[80]. The KEGG (https://www.genome.jp/kegg/)[81] database was used to integrate multiomics profiles.

There was, however, a drawback arising from incomplete coverage of the identified metabolome and sparse interaction information between metabolites and expression level data. To deal with this issue, color-coded KEGG pathways using the Pathview R package (v.1.40.0)[82]

were manually curated by visual inspection to find recovered metabolic alteration in the aging model attributed to *Crtc2* AKO.

Single-cell RNA-seq

Libraries for scRNA-seq were generated using Chromium Single Cell 3′ GEM, Library & Gel Bead kit (PN-100092, 10x Genomics), Chromium Single Cell B Chip kit (PN-1000074, 10x Genomics) and Chromium i7 Multiplex kit (PN-120262, 10x Genomics). Briefly, cells were diluted to 7×10^5 to 1.2×10^6 cells ml^{-1} and calculated volume of cells was mixed with master mix containing reverse transcription reagents to recover 6,000 cells per sample. To generate gel bead-in-emulsions (GEMs), samples were loaded onto the chip and following microfluidic process was performed on a Chromium controller (10x Genomics). GEMs were incubated using a thermal cycler to perform reverse transcription. Afterwards, GEMs were broken and pooled cDNA was purified using Silane magnetic beads. Barcoded cDNAs were amplified using a thermal cycler. Subsequent processes for library construction including enzymatic fragmentation, end repair, A-tailing, adaptor ligation and sample index PCR were performed according to the manufacturer's protocol. The size and concentration of cDNA and libraries were analyzed using a Bioanalyzer (Agilent). Libraries were pooled and sequenced through a NovaSeq S4 platform (Illumina) using a paired-end 100-bp protocol to generate minimum 20,000 reads pairs per cell.

scRNA-seq data analysis

Raw reads for scRNA-seq were mapped to the mouse reference genome (GRCm38) and processed using CellRanger (v.3.0.2)[83] with the Ensembl GRCm38.95 GTF file. For each sample, a gene-by-cell UMI count matrix was generated with default parameters except for expect-cells of 6,000. Using the emptyDrops function of the DropletUtils (v.1.61) R package[84], droplets containing cells were identified. To filter out low-quality cells, cells with >10% UMIs assigned to mitochondrial genes and <2.5 log_{10}-scaled total UMI count were excluded after calculation of QC factors using the calculateQCMetrics function of the scater (v.1.14.6) R package[85]. Then, each sample was aggregated into a single count matrix. To normalize cell-specific biases, cells were clustered using the quickCluster function of the scran (v.1.0.2) R package[86] and cell-specific size factors were calculated using the computeSumFactors function of the same package. Raw UMI counts were normalized by size factors and then log_2-transformed with a pseudocount of 1. All cells were clustered into 35 clusters using the FindClusters function of the Seurat (v.3.1.5) R package[87,88] on the first 15 principal components of highly variable genes with resolution of 0.8. Cells were visualized on a two-dimensional UMAP plot using the RunUMAP function. Lymphoid cells, myeloid cells and AP cells were further clustered by the top 8, 10 and 15 principal components of 1,000 highly variable genes, respectively. Odds ratios and associated *P* values of cell-type proportion changes between conditions were evaluated with the mixed-effects models using the glmer function of the lme4 (v.1.1.25) R package[89]. The pseudotime analysis was performed using the Palantir (v.0.2.6) Python package[90]. For the Palantir *t*-SNE plots, diffusion components were computed using the run_diffusion_maps function with the first 100 principal components. Then, a *k*-nearest neighbor graph was constructed with $k = 30$ using the first ten diffusion components. Cells were visualized using the run_tsne function with perplexity of 500. GO enrichment analysis was performed using the runTest function of the topGO (v.2.38.1) R package. Cells were assigned into one of two differentiation fates by binomial sampling based on branch probabilities, which were calculated using the run_palantir function. The activity of signaling pathways for each stage was inferred using the progeny function of the progeny (v.1.12.0) R package[91–93]. Ligand–receptor analysis was conducted using the CellphoneDB (v.2.0.0) Python package[94] for each condition. The normalized expression and the assigned cell type for each cell was used for inferring the ligand–receptor pair. Pairs with $P < 0.05$ were analyzed as significant pairs.

Publication license for illustration

Parts of figures in this work were generated using BioRender under the publication license.

Statistical analyses

No statistical methods were used to predetermine sample size but our sample sizes are similar to those reported in previous publications[16–18]. We provided individual data points assuming that data distribution was normal but this was not formally tested. The littermate mice were selected for each experimental condition and the investigators were not blinded to allocation during experiments and outcome assessment. We did not exclude data points from the analyses.

Data were analyzed using Prism (GraphPad v.8.0, GraphPad Software) and presented as mean ± s.e.m. or s.d. Statistical significance was determined using a Student's *t*-test or one-way ANOVA as indicated in the figure legends.

Reporting summary

Further information on research design is available in the Nature Portfolio Reporting Summary linked to this article.

Data availability

All the data supporting this work are available as Source Data or Supplementary Information. The data for the mRNA-seq and scRNA-seq were deposited in the National Cancer Center for Biotechnology Information (accession nos. GSE207433 (for mRNA-seq) and PRJNA852570 (for scRNA-seq)). Processed data for mRNA-seq were also deposited in the same location. Processed data for the scRNA-seq are available at https://doi.org/10.5281/zenodo.7949695. MS/MS patterns from features were identified by comparing the experimental data against the METLIN (metlin.scripps.edu) database and the KEGG (https://www.genome.jp/kegg/) database was used to integrate multiomics profiles.

Code availability

Analysis scripts for scRNA-seq data are available at https://github.com/CB-postech/NATURE-AGING-adipose-CRTC2.

References

1. Liu, Z., Wu, K. K. L., Jiang, X., Xu, A. & Cheng, K. K. Y. The role of adipose tissue senescence in obesity- and ageing-related metabolic disorders. *Clin. Sci.* **134**, 315–330 (2020).
2. Martyniak, K. & Masternak, M. M. Changes in adipose tissue cellular composition during obesity and aging as a cause of metabolic dysregulation. *Exp. Gerontol.* **94**, 59–63 (2017).
3. Stout, M. B., Justice, J. N., Nicklas, B. J. & Kirkland, J. L. Physiological aging: links among adipose tissue dysfunction, diabetes, and frailty. *Physiology* **32**, 9–19 (2017).
4. Sethi, J. K. & Vidal-Puig, A. J. Thematic review series: adipocyte biology. Adipose tissue function and plasticity orchestrate nutritional adaptation. *J. Lipid Res.* **48**, 1253–1262 (2007).
5. Tchkonia, T. et al. Fat tissue, aging, and cellular senescence. *Aging Cell* **9**, 667–684 (2010).
6. Palmer, A. K. et al. Targeting senescent cells alleviates obesity-induced metabolic dysfunction. *Aging Cell* **18**, e12950 (2019).
7. Coppe, J. P. et al. Senescence-associated secretory phenotypes reveal cell-nonautonomous functions of oncogenic RAS and the p53 tumor suppressor. *PLoS Biol.* **6**, 2853–2868 (2008).
8. Coppe, J. P. et al. A human-like senescence-associated secretory phenotype is conserved in mouse cells dependent on physiological oxygen. *PLoS ONE* **5**, e9188 (2010).
9. Xu, M. et al. Targeting senescent cells enhances adipogenesis and metabolic function in old age. *eLife* **4**, e12997 (2015).
10. Han, H. S., Kwon, Y. & Koo, S. H. Role of CRTC2 in metabolic homeostasis: key regulator of whole-body energy metabolism. *Diabetes Metab. J.* **44**, 498–508 (2020).

11. Koo, S. H. et al. The CREB coactivator TORC2 is a key regulator of fasting glucose metabolism. *Nature* **437**, 1109–1111 (2005).
12. Lee, M. W. et al. Regulation of hepatic gluconeogenesis by an ER-bound transcription factor, CREBH. *Cell Metab.* **11**, 331–339 (2010).
13. Wang, Y., Vera, L., Fischer, W. H. & Montminy, M. The CREB coactivator CRTC2 links hepatic ER stress and fasting gluconeogenesis. *Nature* **460**, 534–537 (2009).
14. Li, Y. et al. A novel role for CRTC2 in hepatic cholesterol synthesis through SREBP-2. *Hepatology* **66**, 481–497 (2017).
15. Han, J. et al. The CREB coactivator CRTC2 controls hepatic lipid metabolism by regulating SREBP1. *Nature* **524**, 243–246 (2015).
16. Han, H. S., Choi, B. H., Kim, J. S., Kang, G. & Koo, S. H. Hepatic Crtc2 controls whole body energy metabolism via a miR-34a-Fgf21 axis. *Nat. Commun.* **8**, 1878 (2017).
17. Han, H. S. et al. A novel role of CRTC2 in promoting nonalcoholic fatty liver disease. *Mol. Metab.* **55**, 101402 (2022).
18. Lee, J. H., Wen, X., Cho, H. & Koo, S. H. CREB/CRTC2 controls GLP-1-dependent regulation of glucose homeostasis. *FASEB J.* **32**, 1566–1578 (2018).
19. Blanchet, E. et al. Feedback inhibition of CREB signaling promotes β cell dysfunction in insulin resistance. *Cell Rep.* **10**, 1149–1157 (2015).
20. Song, Y. et al. CRTC3 links catecholamine signalling to energy balance. *Nature* **468**, 933–939 (2010).
21. Yoon, Y. S. et al. cAMP-inducible coactivator CRTC3 attenuates brown adipose tissue thermogenesis. *PNAS* **115**, E5289–E5297 (2018).
22. Mair, W. et al. Lifespan extension induced by AMPK and calcineurin is mediated by CRTC-1 and CREB. *Nature* **470**, 404–408 (2011).
23. Burkewitz, K. et al. Neuronal CRTC-1 governs systemic mitochondrial metabolism and lifespan via a catecholamine signal. *Cell* **160**, 842–855 (2015).
24. Kevin Flurkey, J. M. C., D.E. Harrison. in *The Mouse in Biomedical Research* Vol. III Ch. 20, 637–672 (Elsevier, 2007).
25. Petkevicius, K. et al. Accelerated phosphatidylcholine turnover in macrophages promotes adipose tissue inflammation in obesity. *eLife* **8**, e47990 (2019).
26. Yoo, H., Antoniewicz, M. R., Stephanopoulos, G. & Kelleher, J. K. Quantifying reductive carboxylation flux of glutamine to lipid in a brown adipocyte cell line. *J. Biol. Chem.* **283**, 20621–20627 (2008).
27. Wurtz, P. et al. Metabolic signatures of insulin resistance in 7,098 young adults. *Diabetes* **61**, 1372–1380 (2012).
28. Newgard, C. B. et al. A branched-chain amino acid-related metabolic signature that differentiates obese and lean humans and contributes to insulin resistance. *Cell Metab.* **9**, 311–326 (2009).
29. Newgard, C. B. Interplay between lipids and branched-chain amino acids in development of insulin resistance. *Cell Metab.* **15**, 606–614 (2012).
30. Olson, K. C., Chen, G., Xu, Y., Hajnal, A. & Lynch, C. J. Alloisoleucine differentiates the branched-chain aminoacidemia of Zucker and dietary obese rats. *Obesity* **22**, 1212–1215 (2014).
31. Zhou, M. et al. Targeting BCAA catabolism to treat obesity-associated insulin resistance. *Diabetes* **68**, 1730–1746 (2019).
32. Solon-Biet, S. M. et al. Branched chain amino acids impact health and lifespan indirectly via amino acid balance and appetite control. *Nat. Metab.* **1**, 532–545 (2019).
33. Richardson, N. E. et al. Lifelong restriction of dietary branched-chain amino acids has sex-specific benefits for frailty and lifespan in mice. *Nat. Aging* **1**, 73–86 (2021).
34. Lackey, D. E. et al. Regulation of adipose branched-chain amino acid catabolism enzyme expression and cross-adipose amino acid flux in human obesity. *Am. J. Physiol. Endocrinol. Metab.* **304**, E1175–E1187 (2013).
35. Herman, M. A., She, P., Peroni, O. D., Lynch, C. J. & Kahn, B. B. Adipose tissue branched chain amino acid (BCAA) metabolism modulates circulating BCAA levels. *J. Biol. Chem.* **285**, 11348–11356 (2010).
36. Takashima, M. et al. Role of KLF15 in regulation of hepatic gluconeogenesis and metformin action. *Diabetes* **59**, 1608–1615 (2010).
37. Blanchard, P. G. et al. PPARγ is a major regulator of branched-chain amino acid blood levels and catabolism in white and brown adipose tissues. *Metabolism* **89**, 27–38 (2018).
38. Herzig, S. et al. CREB controls hepatic lipid metabolism through nuclear hormone receptor PPAR-γ. *Nature* **426**, 190–193 (2003).
39. Chen, C., Zhou, M., Ge, Y. & Wang, X. SIRT1 and aging related signaling pathways. *Mech. Ageing Dev.* **187**, 111215 (2020).
40. Lamming, D. W. & Sabatini, D. M. A central role for mTOR in lipid homeostasis. *Cell Metab.* **18**, 465–469 (2013).
41. Van Skike, C. E. et al. mTOR drives cerebrovascular, synaptic, and cognitive dysfunction in normative aging. *Aging Cell* **19**, e13057 (2020).
42. Zhao, X. et al. Metformin protects PC12 cells and hippocampal neurons from H_2O_2-induced oxidative damage through activation of AMPK pathway. *J. Cell Physiol.* https://doi.org/10.1002/jcp.28337 (2019).
43. Satoh, A. et al. Sirt1 extends life span and delays aging in mice through the regulation of Nk2 homeobox 1 in the DMH and LH. *Cell Metab.* **18**, 416–430 (2013).
44. Lee, J. et al. A pathway involving farnesoid X receptor and small heterodimer partner positively regulates hepatic sirtuin 1 levels via microRNA-34a inhibition. *J. Biol. Chem.* **285**, 12604–12611 (2010).
45. Lannes, J. et al. Rapid communication: a microRNA-132/212 pathway mediates GnRH activation of FSH expression. *Mol. Endocrinol.* **29**, 364–372 (2015).
46. Vasa-Nicotera, M. et al. miR-146a is modulated in human endothelial cell with aging. *Atherosclerosis* **217**, 326–330 (2011).
47. Vo, N. et al. A cAMP-response element binding protein-induced microRNA regulates neuronal morphogenesis. *PNAS* **102**, 16426–16431 (2005).
48. Yoon, M. S. & Choi, C. S. The role of amino acid-induced mammalian target of rapamycin complex 1(mTORC1) signaling in insulin resistance. *Exp. Mol. Med.* **48**, e201 (2016).
49. Herzig, S. & Shaw, R. J. AMPK: guardian of metabolism and mitochondrial homeostasis. *Nat. Rev. Mol. Cell Biol.* **19**, 121–135 (2018).
50. Lumeng, C. N. et al. Aging is associated with an increase in T cells and inflammatory macrophages in visceral adipose tissue. *J. Immunol.* **187**, 6208–6216 (2011).
51. Carter, S. et al. Loss of OcaB prevents age-induced fat accretion and insulin resistance by altering B-lymphocyte transition and promoting energy expenditure. *Diabetes* **67**, 1285–1296 (2018).
52. Camell, C. D. et al. Aging induces an Nlrp3 inflammasome-dependent expansion of adipose B cells that impairs metabolic homeostasis. *Cell Metab.* **30**, 1024–1039 (2019).
53. Bapat, S. P. et al. Depletion of fat-resident Treg cells prevents age-associated insulin resistance. *Nature* **528**, 137–141 (2015).
54. Chakarov, S. et al. Two distinct interstitial macrophage populations coexist across tissues in specific subtissular niches. *Science* **363**, eaau0964 (2019).
55. Jaitin, D. A. et al. Lipid-associated macrophages control metabolic homeostasis in a Trem2-dependent manner. *Cell* **178**, 686–698 (2019).

56. Hill, D. A. et al. Distinct macrophage populations direct inflammatory versus physiological changes in adipose tissue. *PNAS* **115**, E5096–E5105 (2018).
57. Pirzgalska, R. M. et al. Sympathetic neuron-associated macrophages contribute to obesity by importing and metabolizing norepinephrine. *Nat. Med.* **23**, 1309–1318 (2017).
58. Merrick, D. et al. Identification of a mesenchymal progenitor cell hierarchy in adipose tissue. *Science* https://doi.org/10.1126/science.aav2501 (2019).
59. Nahmgoong, H. et al. Distinct properties of adipose stem cell subpopulations determine fat depot-specific characteristics. *Cell metabolism* **34**, 458–472 e456 (2022).
60. Fuster, J. J. et al. Noncanonical Wnt signaling promotes obesity-induced adipose tissue inflammation and metabolic dysfunction independent of adipose tissue expansion. *Diabetes* **64**, 1235–1248 (2015).
61. Trayhurn, P. Hypoxia and adipose tissue function and dysfunction in obesity. *Physiol. Rev.* **93**, 1–21 (2013).
62. Datta, R., Podolsky, M. J. & Atabai, K. Fat fibrosis: friend or foe? *JCI Insight* https://doi.org/10.1172/jci.insight.122289 (2018).
63. Hu, L. et al. IGF1 promotes adipogenesis by a lineage bias of endogenous adipose stem/progenitor cells. *Stem Cells* **33**, 2483–2495 (2015).
64. Eguchi, J. et al. Interferon regulatory factors are transcriptional regulators of adipogenesis. *Cell Metab.* **7**, 86–94 (2008).
65. Zhu, W., Zhao, M., Mattapally, S., Chen, S. & Zhang, J. CCND2 overexpression enhances the regenerative potency of human induced pluripotent stem cell-derived cardiomyocytes: remuscularization of injured ventricle. *Circ. Res.* **122**, 88–96 (2018).
66. Jun, J. I. & Lau, L. F. The matricellular protein CCN1 induces fibroblast senescence and restricts fibrosis in cutaneous wound healing. *Nat. Cell Biol.* **12**, 676–685 (2010).
67. Arcidiacono, B. et al. Expression of matrix metalloproteinase-11 is increased under conditions of insulin resistance. *World J. Diabetes* **8**, 422–428 (2017).
68. Ohta, H. & Itoh, N. Roles of FGFs as adipokines in adipose tissue development, remodeling, and metabolism. *Front. Endocrinol.* **5**, 18 (2014).
69. Laberge, R. M. et al. MTOR regulates the pro-tumorigenic senescence-associated secretory phenotype by promoting IL1A translation. *Nat. Cell Biol.* **17**, 1049–1061 (2015).
70. Viola, A. & Luster, A. D. Chemokines and their receptors: drug targets in immunity and inflammation. *Annu. Rev. Pharmacol. Toxicol.* **48**, 171–197 (2008).
71. Yoon, Y. S. et al. Activation of the adipocyte CREB/CRTC pathway in obesity. *Commun. Biol.* **4**, 1214 (2021).
72. Tchkonia, T. et al. Increased TNFα and CCAAT/enhancer-binding protein homologous protein with aging predispose preadipocytes to resist adipogenesis. *Am. J. Physiol. Endocrinol. Metab.* **293**, E1810–E1819 (2007).
73. Lynch, C. J. & Adams, S. H. Branched-chain amino acids in metabolic signalling and insulin resistance. *Nat. Rev. Endocrinol.* **10**, 723–736 (2014).
74. Blanchard, P. G. et al. Major involvement of mTOR in the PPARγ-induced stimulation of adipose tissue lipid uptake and fat accretion. *J. Lipid Res.* **53**, 1117–1125 (2012).
75. Leibowitz, G., Cerasi, E. & Ketzinel-Gilad, M. The role of mTOR in the adaptation and failure of β-cells in type 2 diabetes. *Diabetes Obes. Metab.* **10**, 157–169 (2008).
76. Magkos, F. et al. Effect of Roux-en-Y gastric bypass and laparoscopic adjustable gastric banding on branched-chain amino acid metabolism. *Diabetes* **62**, 2757–2761 (2013).
77. Choi, S. et al. Depletion of Prmt1 in adipocytes impairs glucose homeostasis in diet-induced obesity. *Diabetes* **70**, 1664–1678 (2021).
78. Lee, H. et al. Prominin-1-radixin axis controls hepatic gluconeogenesis by regulating PKA activity. *EMBO Rep.* **21**, e49416 (2020).
79. Storey, J. D. & Tibshirani, R. Statistical significance for genomewide studies. *PNAS* **100**, 9440–9445 (2003).
80. Young, M. D., Wakefield, M. J., Smyth, G. K. & Oshlack, A. Gene Ontology analysis for RNA-seq: accounting for selection bias. *Genome Biol.* **11**, R14 (2010).
81. Ogata, H. et al. KEGG: Kyoto Encyclopedia of Genes and Genomes. *Nucleic Acids Res.* **27**, 29–34 (1999).
82. Luo, W. & Brouwer, C. Pathview: an R/Bioconductor package for pathway-based data integration and visualization. *Bioinformatics* **29**, 1830–1831 (2013).
83. Zheng, G. X. et al. Massively parallel digital transcriptional profiling of single cells. *Nat. Commun.* **8**, 14049 (2017).
84. Lun, A. T. L. et al. EmptyDrops: distinguishing cells from empty droplets in droplet-based single-cell RNA sequencing data. *Genome Biol.* **20**, 63 (2019).
85. McCarthy, D. J., Campbell, K. R., Lun, A. T. & Wills, Q. F. Scater: pre-processing, quality control, normalization and visualization of single-cell RNA-seq data in R. *Bioinformatics* **33**, 1179–1186 (2017).
86. Lun, A. T., McCarthy, D. J. & Marioni, J. C. A step-by-step workflow for low-level analysis of single-cell RNA-seq data with Bioconductor. *F1000Res* **5**, 2122 (2016).
87. Butler, A., Hoffman, P., Smibert, P., Papalexi, E. & Satija, R. Integrating single-cell transcriptomic data across different conditions, technologies, and species. *Nat. Biotechnol.* **36**, 411–420 (2018).
88. Sonntag, T. et al. Mitogenic signals stimulate the CREB coactivator CRTC3 through PP2A recruitment. *iScience* **11**, 134–145 (2019).
89. Fonseka, C. Y. et al. Mixed-effects association of single cells identifies an expanded effector CD4(+) T cell subset in rheumatoid arthritis. *Sci. Transl. Med.* **10**, eaaq0305 (2018).
90. Setty, M. et al. Characterization of cell fate probabilities in single-cell data with Palantir. *Nat. Biotechnol.* **37**, 451–460 (2019).
91. Holland, C. H. et al. Robustness and applicability of transcription factor and pathway analysis tools on single-cell RNA-seq data. *Genome Biol.* **21**, 36 (2020).
92. Holland, C. H., Szalai, B. & Saez-Rodriguez, J. Transfer of regulatory knowledge from human to mouse for functional genomics analysis. *Biochim. Biophys. Acta Gene Regul. Mech.* **1863**, 194431 (2020).
93. Schubert, M. et al. Perturbation-response genes reveal signaling footprints in cancer gene expression. *Nat. Commun.* **9**, 20 (2018).
94. Efremova, M., Vento-Tormo, M., Teichmann, S. A. & Vento-Tormo, R. CellPhoneDB: inferring cell–cell communication from combined expression of multi-subunit ligand–receptor complexes. *Nat. Protoc.* **15**, 1484–1506 (2020).

Acknowledgements

This research was supported by a National Research Foundation of Korea grant funded by the Korean Government (MSIT) (NRF-2019M3A9D5A01102794 and NRF-2021R1A2C3003435 (to S.H.K.), NRF-2020R1A2C2007835 (to G.S.H.), NRF-2021M3H9A1030158 (to J.K.K.) and NRF-2021R1A2C2003171 (to M.H.M.)). G.S.H. was supported by the Korea Basic Science Institute (C370000). H.S.H. was supported by NRF-2018R1A6A3A11043165. S.H.K. was supported by a grant from Korea University. The funders had no role in study design,

data collection and analysis, decision to publish or preparation of the manuscript.

Author contributions

S.H.K., G.S.H. and J.K.K. conceived the idea and developed the study design. H.S.H., E.A., E.S.P., T.H., S.C., Y.K., B.H.C., J.L., Y.H.C., Y.L.J., G.B.L. and M.K. performed experiments and analyzed the data. H.S.H., E.A., E.S.P., J.K.S., H.M.S., H.R.K., M.H.M., J.K.S., G.S.H., K.W.C. and S.H.K. interpreted data and H.S.H., E.A., E.S.P., J.K.K., G.S.H. and S.H.K wrote the manuscript.

Competing interests

The authors declare no competing interests.

Additional information

Extended data is available for this paper at https://doi.org/10.1038/s43587-023-00460-8.

Supplementary information The online version contains supplementary material available at https://doi.org/10.1038/s43587-023-00460-8.

Correspondence and requests for materials should be addressed to Jong Kyoung Kim, Geum-Sook Hwang or Seung-Hoi Koo.

Peer review information *Nature Aging* thanks the anonymous reviewers for their contribution to the peer review of this work.

https://doi.org/10.1038/s43587-023-00460-8

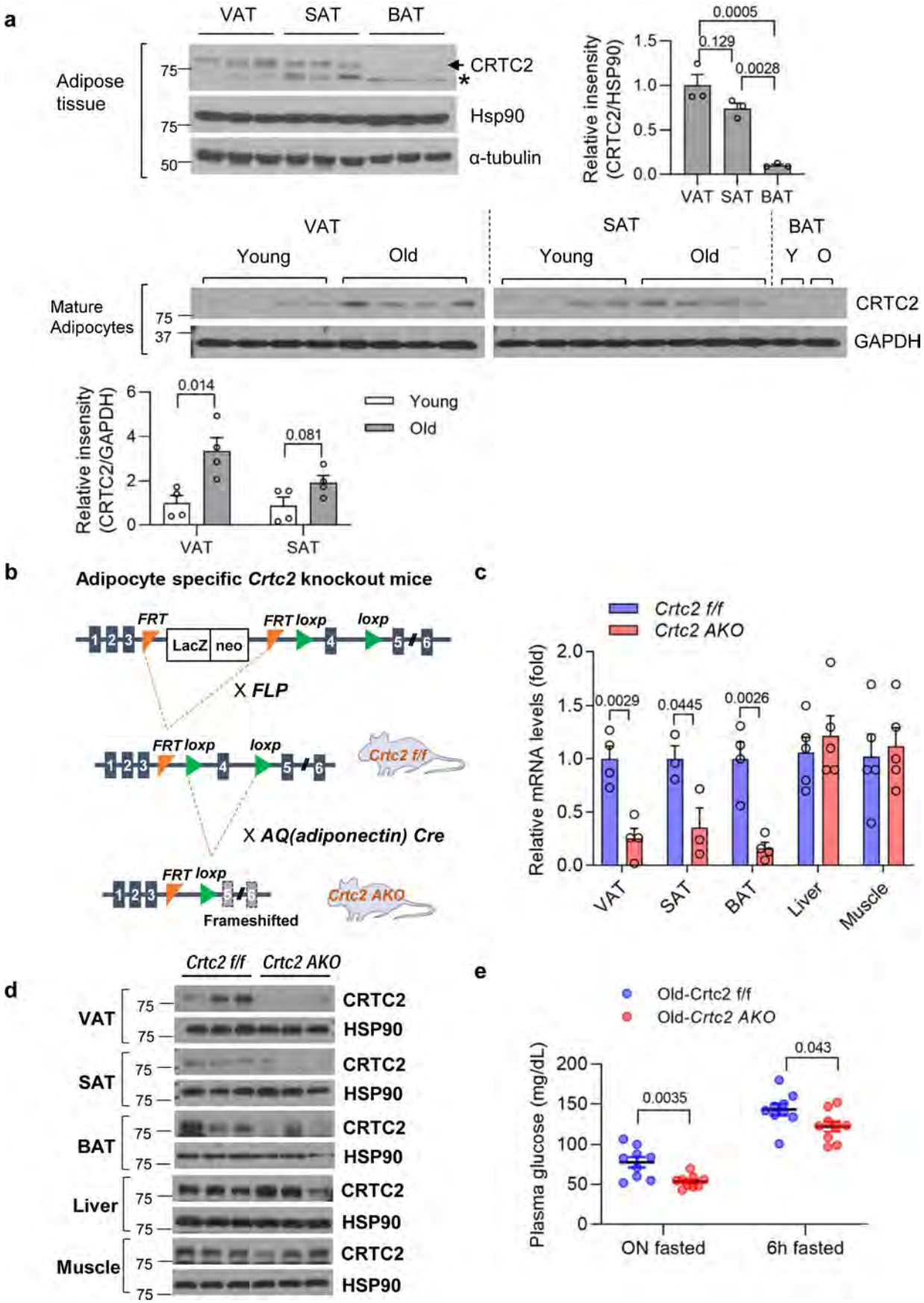

Extended Data Fig. 1 | See next page for caption.

https://doi.org/10.1038/s43587-023-00460-8

Extended Data Fig. 1 | Age-induced expression of CRTC2 in VAT affects energy homeostasis. a. A representative western blot analysis showing relative expression of CRTC2 among the adipose tissues (3-month-old mice) (top). *: non-specific band. The quantitation of CRTC2 bands was also shown (n = 3 mice per group). A representative western blot analysis showing effects of aging on CRTC2 expression in mature adipocytes from VAT, SAT, and BAT (3-month-old mice and 18-month-old mice, n = 4 mice per group for VAT and SAT, and n = 1 mouse for BAT) (bottom). The quantitation of CRTC2 bands from mature adipocytes of VAT and SAT was also shown. **b**. Schematic diagram showing the targeting strategy for generating adipocyte-specific *Crtc2* knockout mice. **c** and **d**. Confirmation of adipocyte-specific depletion of *Crtc2* in *Crtc2* AKO mice. mRNA levels (**c**, QPCR) and protein levels (**d**, a representative western blot analysis) of *Crtc2* in metabolic tissues showing the specificity of adipocyte-specific depletion of *Crtc2* in 4 h-fasted, 3-month-old mice under normal chow diet (NCD). N = 4 mice per group for mRNA analysis and n = 3 mice per group for protein analysis. Data in **a** and **c** represent mean ± SEM. *P* values were determined using one-way ANOVA with Tukey's multiple comparisons test (**a**, top) or student's t-test (**a**, bottom and **c**).

https://doi.org/10.1038/s43587-023-00460-8

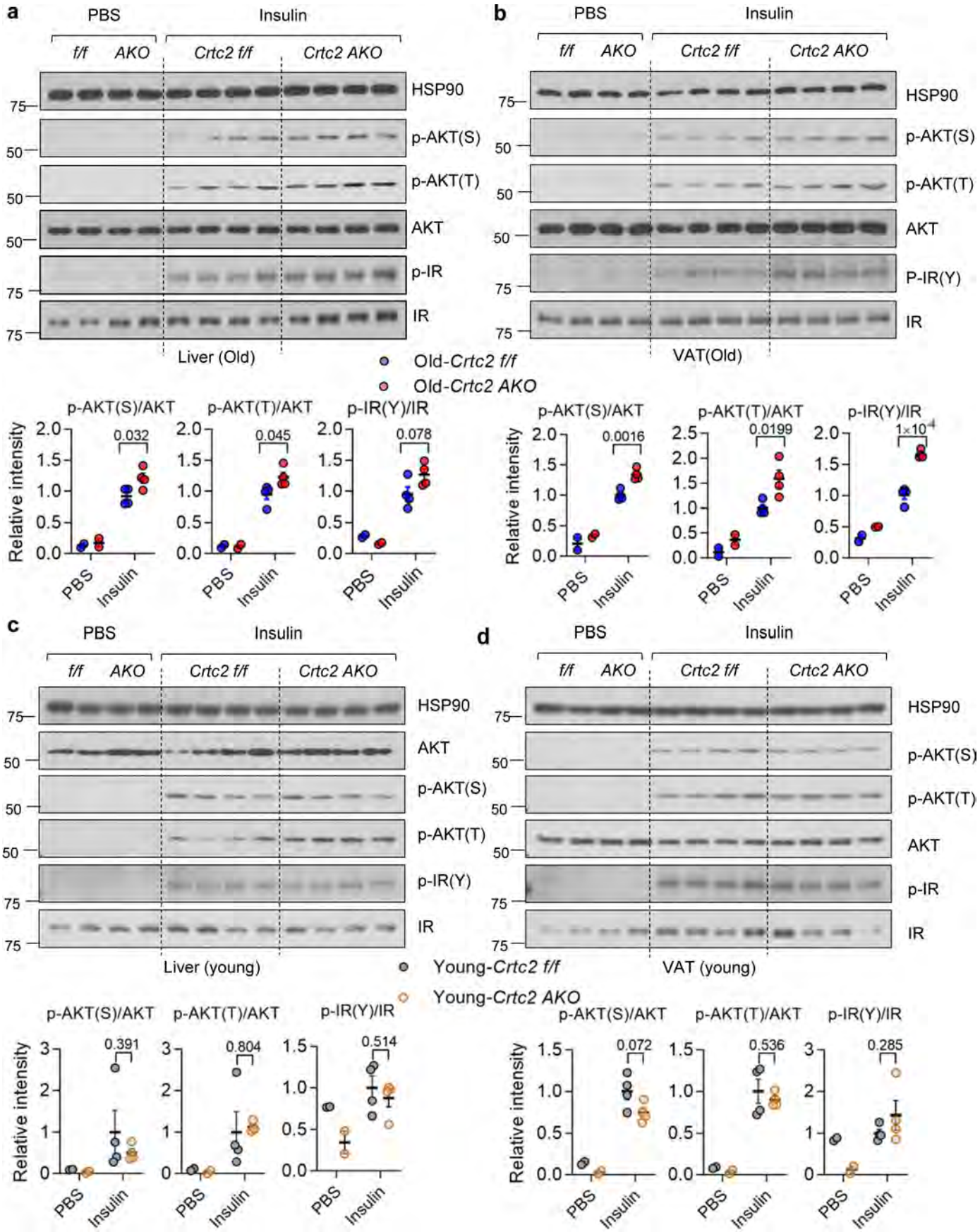

Extended Data Fig. 2 | See next page for caption.

https://doi.org/10.1038/s43587-023-00460-8

Extended Data Fig. 2 | Adipocyte-specific depletion of *Crtc2* restores age-associated changes in insulin signaling. a and **b**. Effects of aging and adipocyte-specific depletion of *Crtc2* on insulin signaling. A representative western blot analysis showing changes in insulin signaling in the liver (**a**) and VAT (**b**) of male young *Crtc2* f/f mice (3-month-old), old *Crtc2* f/f mice (18-month-old), and old *Crtc2* AKO mice (18-month-old). N = 2 mice per group for PBS-injected samples, and n = 4 mice per group for insulin-injected samples. Quantitation of p-AKT(S)/AKT, p-AKT(T)/AKT, and p-IR(Y)/IR were also shown. **c** and **d**. Effects of adipocyte-specific depletion of *Crtc2* on insulin signaling. A representative western blot analysis was shown to measure changes in insulin signaling in the liver (**c**) and VAT (**d**) of male young *Crtc2* f/f mice (3-month-old), and young *Crtc2* AKO mice (3-month-old). N = 2 mice per group for PBS-injected samples, and n = 4 mice per group for insulin-injected samples. Quantitation of p-AKT(S)/AKT, p-AKT(T)/AKT, and p-IR(Y)/IR were also shown. For **a**-**d**, statistical analysis was performed only in insulin-injected samples. Data represent mean ± SEM. *P* values were determined using student's t-test.

https://doi.org/10.1038/s43587-023-00460-8

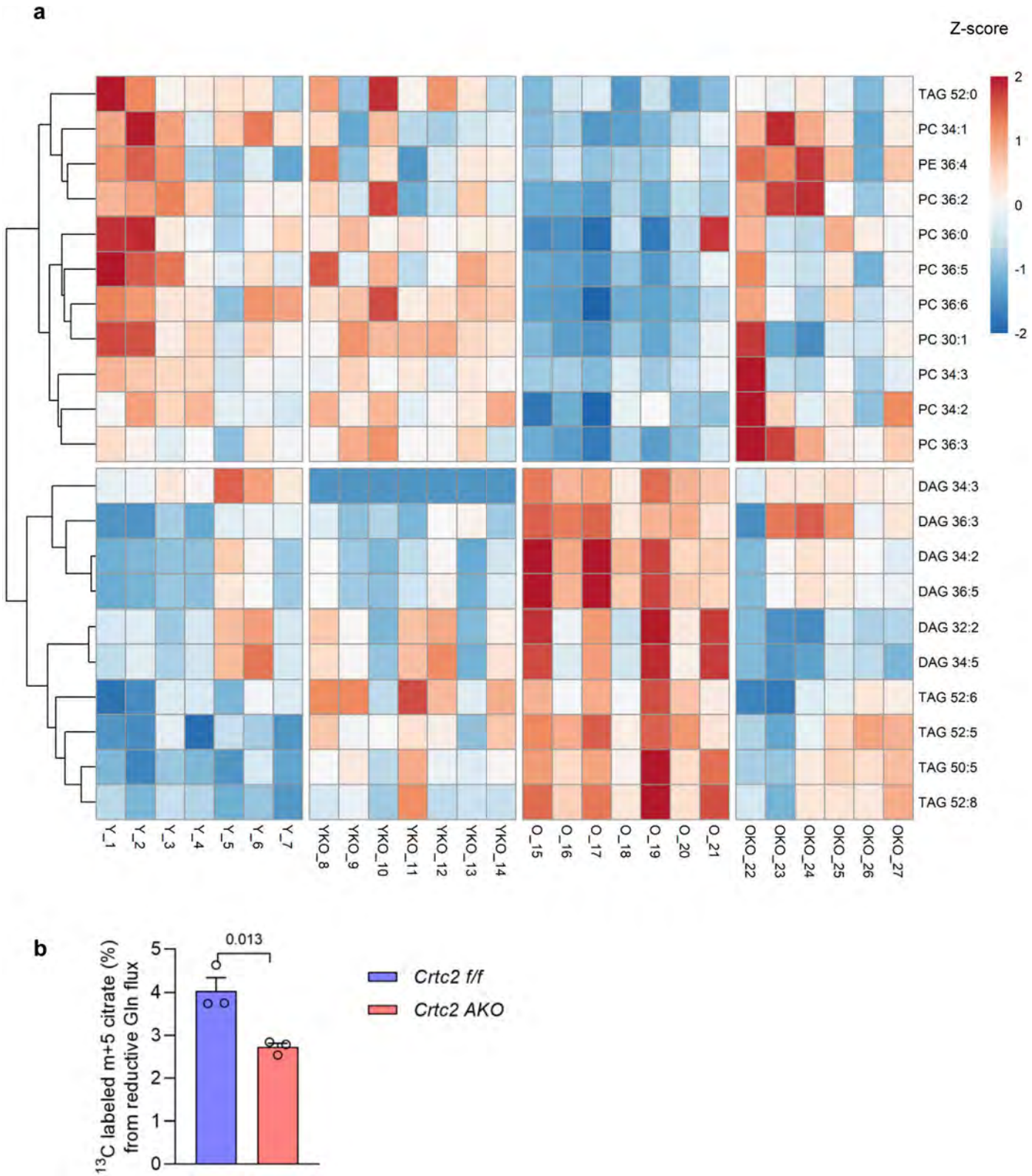

Extended Data Fig. 3 | Adipocyte-specific depletion of *Crtc2* restores age-associated changes in lipid profiles of VAT. Lipid profiling analysis was performed by using male young *Crtc2* f/f mice (3-month-old), young *Crtc2* AKO mice (3-month-old), old *Crtc2* f/f mice (18-month-old), and old *Crtc2* AKO mice (18-month-old). **a.** Lipid profiling analysis of mouse VAT *in vivo* (n = 7 for young *Crtc2* f/f mice, n = 7 for young *Crtc2* AKO mice, n = 7 for old *Crtc2* f/f mice, and n = 6 for old *Crtc2* AKO mice). A heatmap analysis results from significantly differential metabolites (*q*-values from permutation analysis to test the recovery pattern < 0.05). Measured relative intensities are normalized into z-score across samples. Clustered heatmap was drawn by using R package "heatmap". Euclidean distance and complete method were used for the clustering. **b.** Fractional labeling of citrate m + 5 from [U-^{13}C] glutamine via reductive TCA cycle fluxes. Data represent mean ± SEM (n = 3 biological replicates per group). *P* values were determined using student's t-test.

https://doi.org/10.1038/s43587-023-00460-8

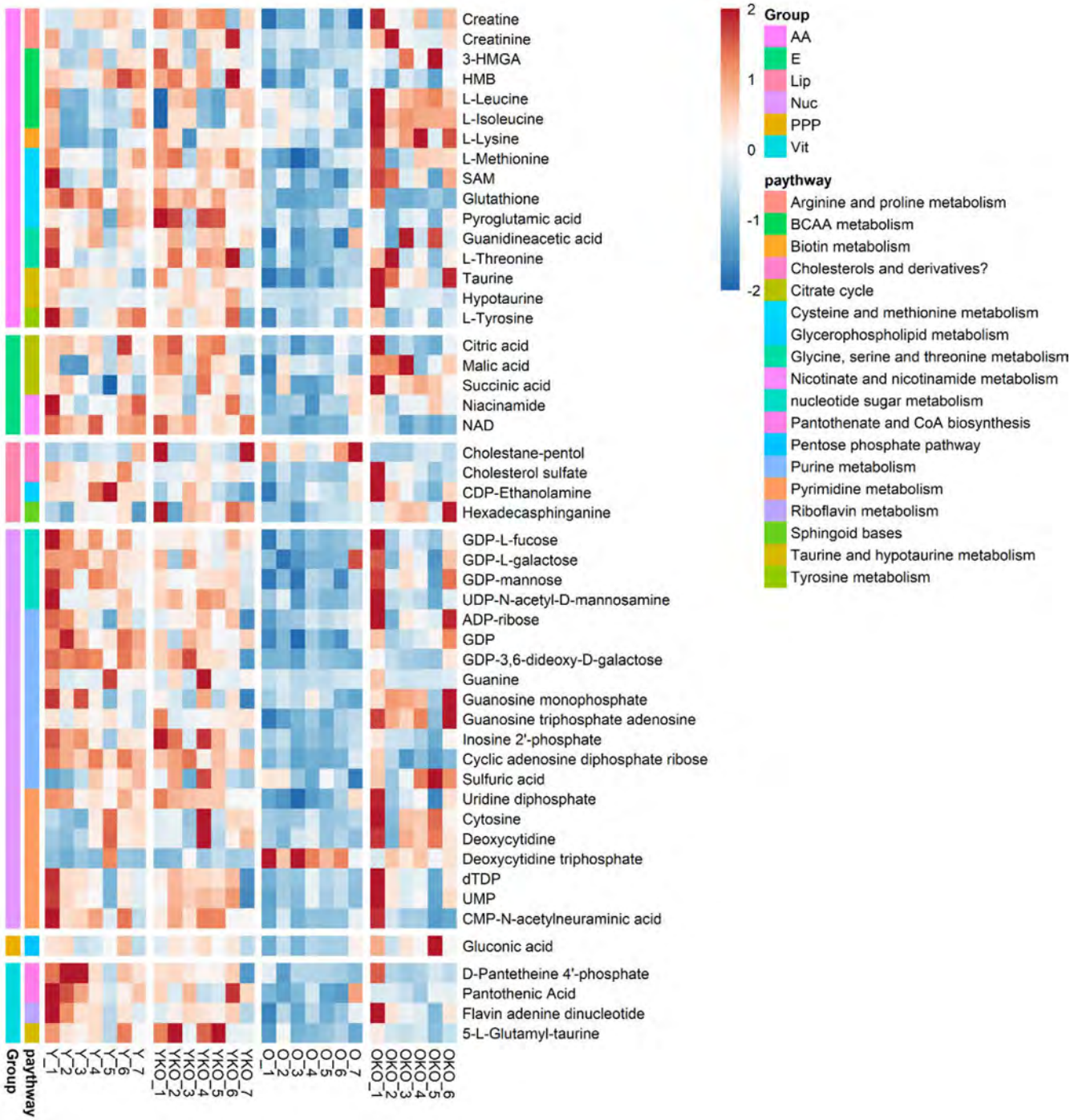

Extended Data Fig. 4 | Adipocyte-specific depletion of *Crtc2* restores age-associated changes in polar metabolome of VAT. Metabolomics analysis was performed by using male young *Crtc2* f/f mice (3-month-old), old *Crtc2* f/f mice (18-month-old), and old *Crtc2* AKO mice (18-month-old). A heatmap of metabolites from mouse VAT *in vivo*, with recovery pattern. Permutation analysis was conducted to detect recovery pattern from metabolic profiling data. Metabolites with *q* value less than 0.05 were plotted and further curated according to their residing KEGG pathways (n = 7 for young *Crtc2* f/f mice, n = 7 for young *Crtc2* AKO mice, n = 7 for old *Crtc2* f/f mice, and n = 6 for old *Crtc2* AKO mice). Measured relative intensities are normalized into z-score across samples.

https://doi.org/10.1038/s43587-023-00460-8

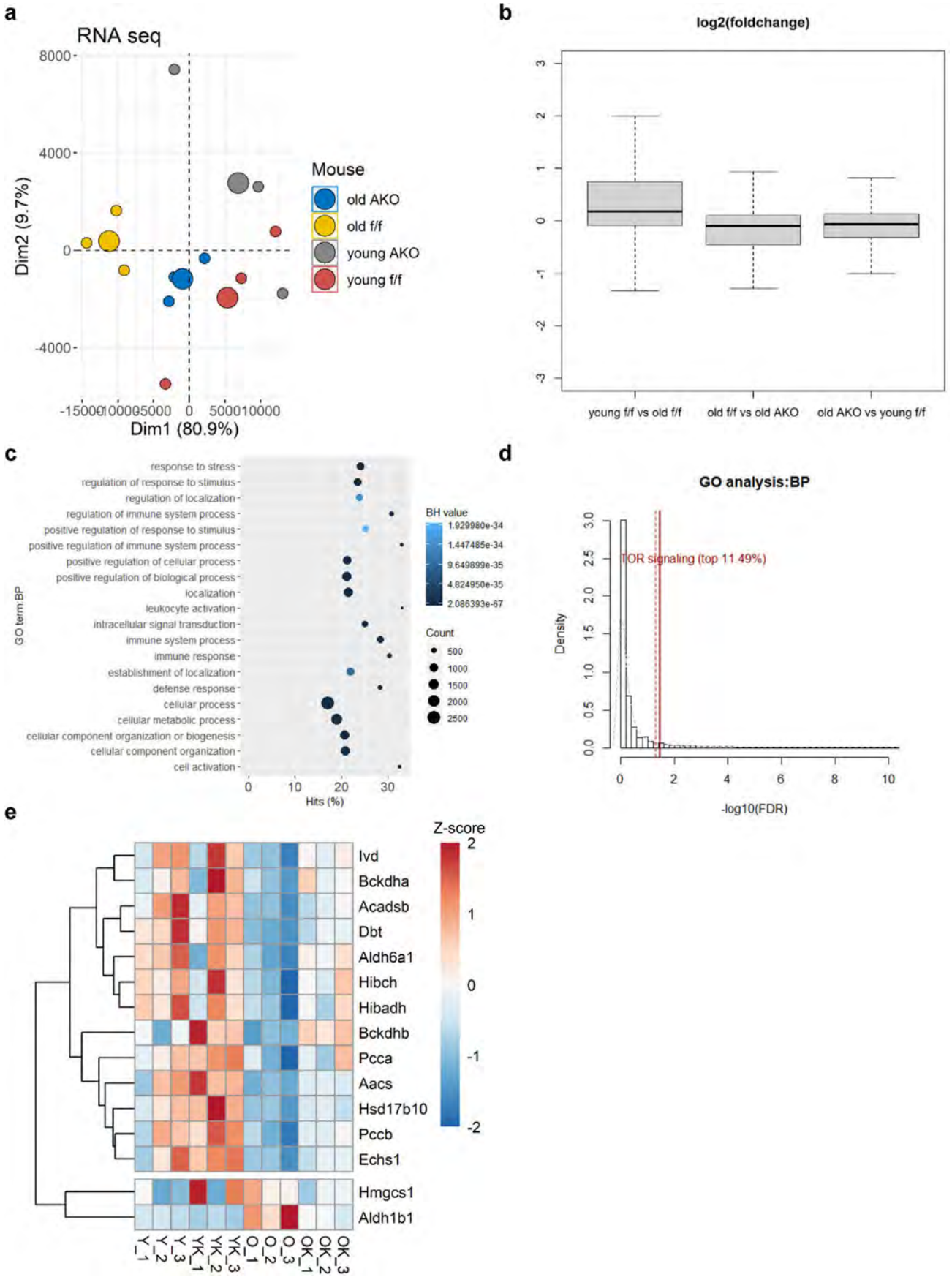

Extended Data Fig. 5 | See next page for caption.

https://doi.org/10.1038/s43587-023-00460-8

Extended Data Fig. 5 | Assessment the effect of aging and adipocyte-specific depletion of *Crtc2* on transcriptome in mature adipocytes. RNA sequencing analysis were performed by using male young *Crtc2* f/f mice (3-month-old), old *Crtc2* f/f mice (18-month-old), and old *Crtc2* AKO mice (18-month-old). **a**. PCA plot of RNA sequencing results (n = 3 mice per group). Each cluster's center was plotted as a bigger circle using the same colors. **b**. Box plot of Log2 transformed fold changes of FPKM values of transcriptomic data. 25%, 75%, and the median were presented in the boxplot with whiskers that were 1.5 times of the inerquantile region (n = 3 mice per group, young f/f vs old f/f (left), old f/f vs old AKO (middle), and old AKO vs young f/f (right)). **c**. GO analysis: Biological Process results of RNA sequencing results (n = 3 mice per group). **d**. Distribution of -log10(FDR) from GO analysis: Biological Process. **e**. RNA sequencing results of genes annotated to mmu00280, BCAA degradation, in KEGG pathway (n = 3 mice per group). Measured FPKM values are normalized into z-score across samples.

https://doi.org/10.1038/s43587-023-00460-8

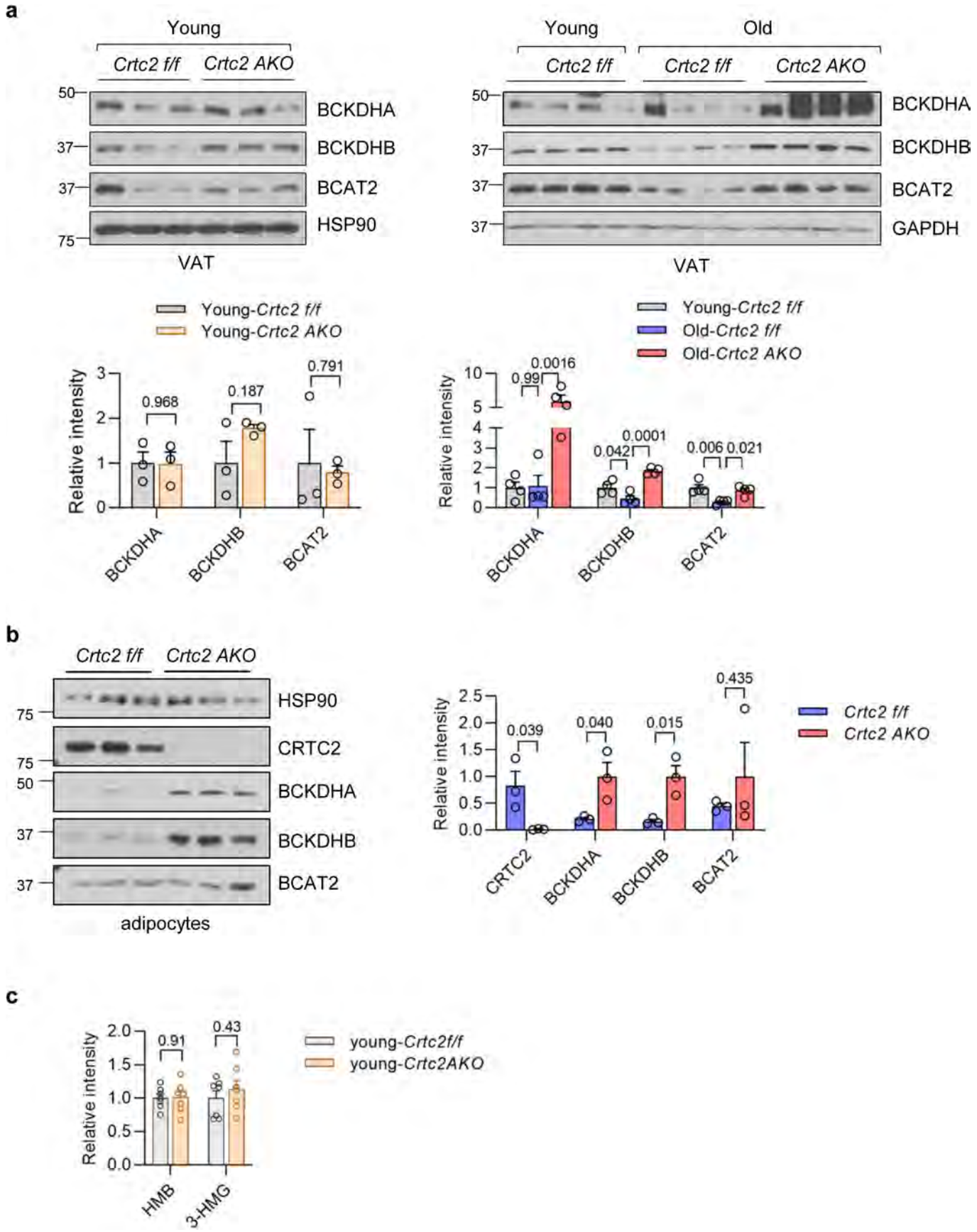

Extended Data Fig. 6 | See next page for caption.

https://doi.org/10.1038/s43587-023-00460-8

Extended Data Fig. 6 | Effects of aging and adipocyte-specific depletion of *Crtc2* on BCAA catabolism. a. A representative western blot analysis showing effects of aging and adipocyte-specific depletion of *Crtc2* on proteins involved in BCAA catabolism in VAT of male young *Crtc2* f/f mice (3-month-old), old *Crtc2* f/f mice (18-month-old), and old *Crtc2* AKO mice (18-month-old). N = 3 mice per group (left) or n = 4 mice per group (right). Relative intensity of specific bands were shown. Data represent mean ± SEM. **b**. A representative western blot analysis showing effects of *Crtc2* deficiency on proteins involved in BCAA catabolism in differentiated immortalized AP cells from *Crtc2* f/f mice and *Crtc2* AKO mice (n = 3 biological replicates per group). Relative intensity of specific bands were shown. Data represent mean ± SEM. **c**. Quantification of HMB and 3-HMG, catabolic intermediates in BCAA metabolism, from VAT of young *Crtc2* f/f mice (3-month-old) and young *Crtc2* AKO mice (3-month-old) (n = 7 biological replicates per group). Data represent mean ± SEM. *P* values were determined using student's t-test (**a** (left), **b**, **c**) or one-way ANOVA with Tukey's multiple comparisons test (**a** (right)).

https://doi.org/10.1038/s43587-023-00460-8

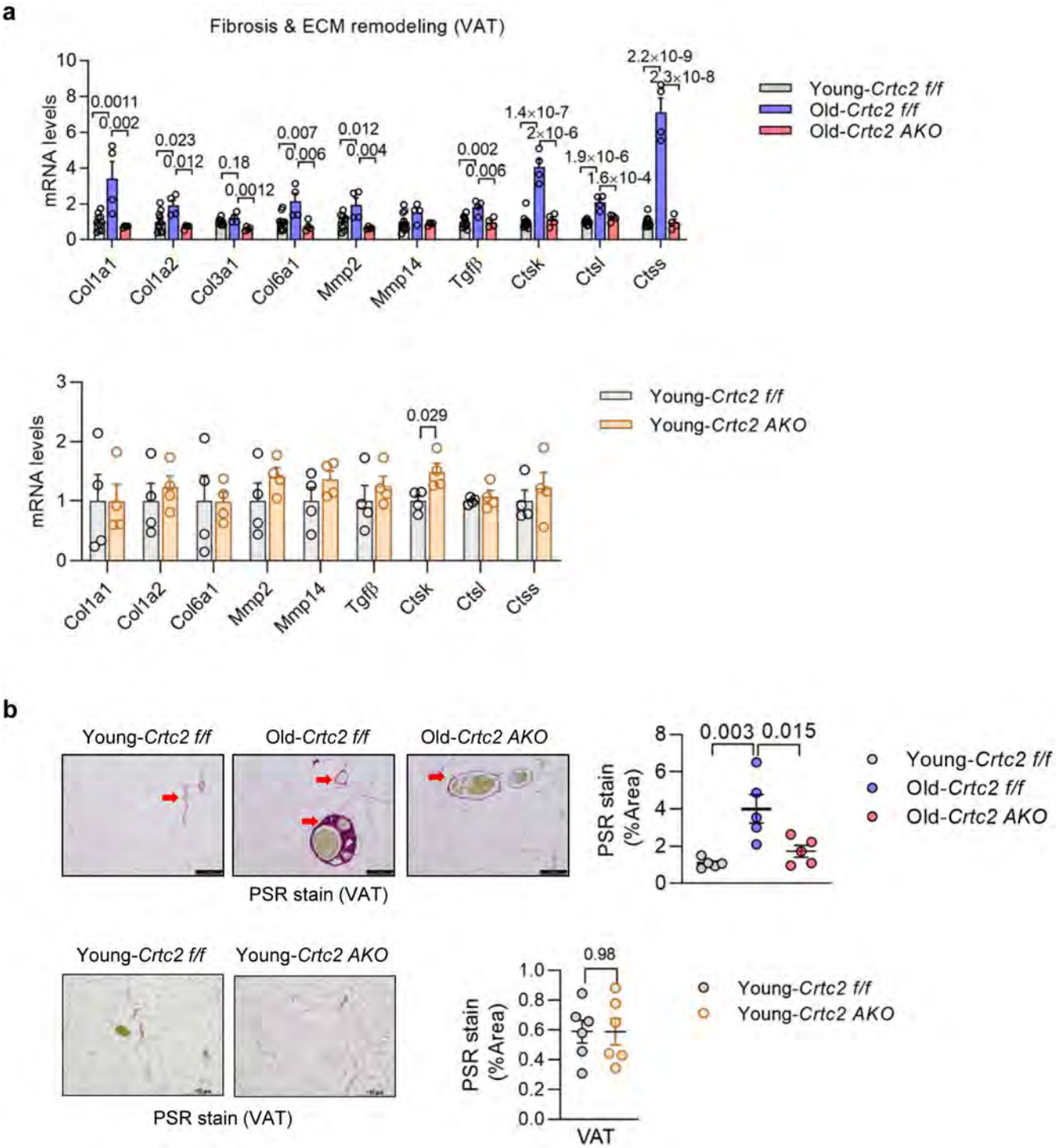

Extended Data Fig. 7 | CRTC2 in adipocytes is critical in age-associated remodeling of VAT. a. QPCR analysis of genes involve in the fibrosis and ECM (extracellular matrix) remodeling in VAT of male young *Crtc2* f/f mice (3-month-old), young *Crtc2* AKO mice (3-month-old), old *Crtc2* f/f mice (18-month-old), and old *Crtc2* AKO mice (18-month-old). Data represent mean ± SEM. For the top figure, n = 10 mice per group for young *Crtc2* f/f mice, n = 4 for old *Crtc2* f/f mice, and n = 4 for old *Crtc2* AKO mice. For the bottom figure, n = 4 mice per group. **b**. A representative Pico Sirius red staining showing effects of aging and adipocyte-specific depletion of *Crtc2* on the fibrotic structure in VAT of male young *Crtc2* f/f mice (3-month-old), young *Crtc2* AKO mice (3-month-old), old *Crtc2* f/f mice (18-month-old), and old *Crtc2* AKO mice (18-month-old) (scale bars, 100 μm (top) or 150 μm (bottom)). N = 5 mice per group (top figure) or n = 6 mice per group (bottom figure). Relative intensity was also shown. Data represent mean ± SEM. *P* values were determined using one-way ANOVA with Tukey's multiple comparisons test (top figures, **a, b**) or student's t-test (bottom figures, **a**, **b**).

https://doi.org/10.1038/s43587-023-00460-8

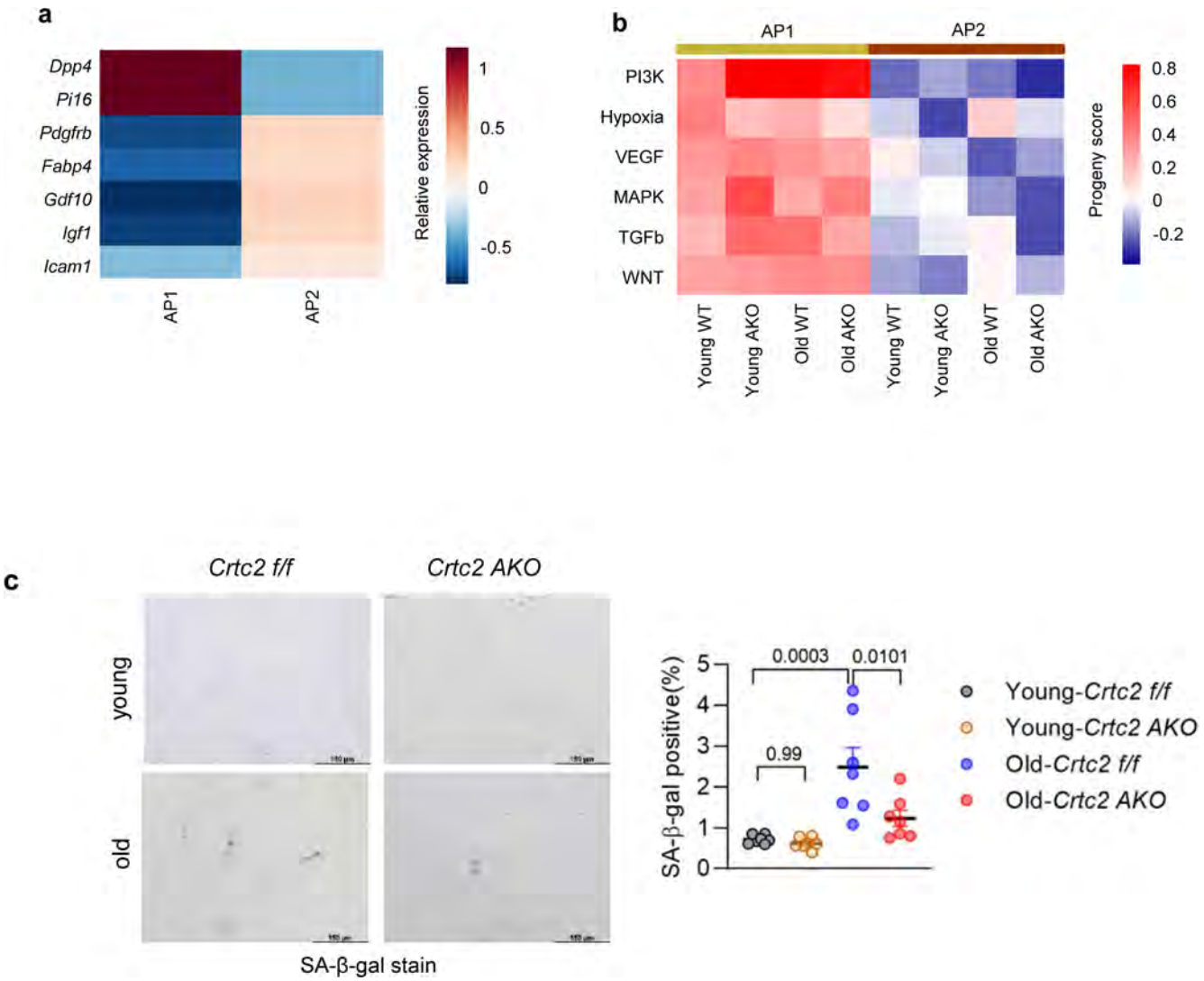

Extended Data Fig. 8 | Effects of aging and adipocyte-specific depletion of *Crtc2* on AP cells in VAT. a. Heatmap showing relative expression of AP subtype marker genes. **b**. Heatmap showing relative pathway activity score of AP subtype across conditions. **c**. Adipocyte progenitor cells (PDGFRα +) isolated from VAT of young Crtc2 f/f mice (3-month-old), young Crtc2 AKO mice (3-mont-old), old Crtc2 f/f mice (20-month-old), and old Crtc2 AKO mice (20-month-old) were analyzed. A representative image showing SA-β-gal staining (scale bars, 150 μm). The staining was performed 1 day after seeding for detecting cellular senescence. Data represent mean ± SEM (n = 7 biological replicates per group). *P* values were determined using one-way ANOVA with Tukey's multiple comparisons test.

https://doi.org/10.1038/s43587-023-00460-8

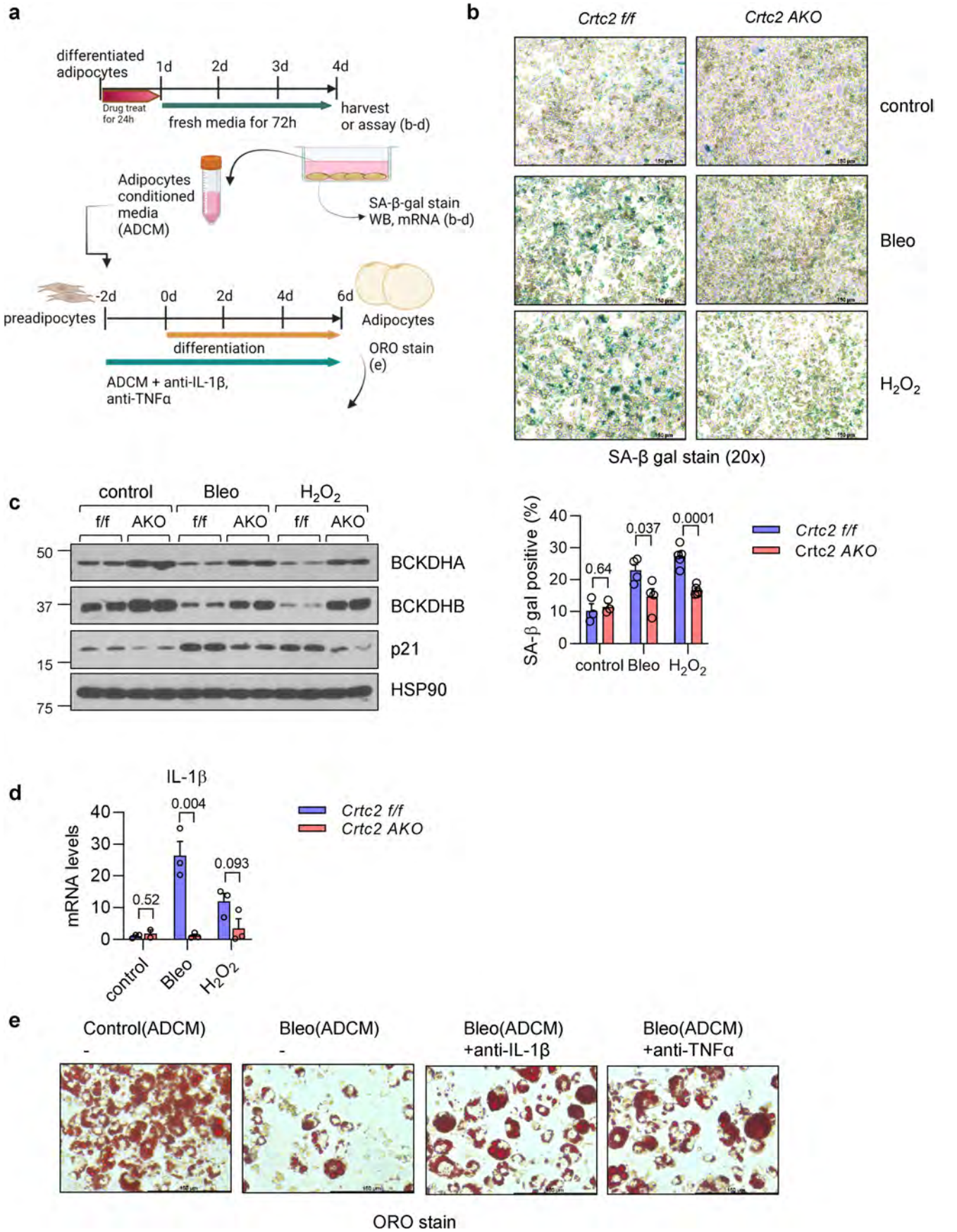

Extended Data Fig. 9 | See next page for caption.

https://doi.org/10.1038/s43587-023-00460-8

Extended Data Fig. 9 | Depletion of *Crtc2* reduced cellular senescence in cultured adipocytes. a. Experimental scheme showing treatment of senescence-inducing agents on differentiated adipocytes that were derived from AP cells of *Crtc2* f/f mice or *Crtc2* AKO mice. **b**. SA-β-gal staining was performed to assess the effect of cellular senescence. A representative image was shown (scale bars, 150 μm). Relative values for SA-β-gal positive cells were also shown. Data represent mean ± SEM (n = 3 biological replicates each control, n = 4 biological replicates each for bleomycin, and n = 5 biological replicates each for H_2O_2). **c**. A representative western blot analysis showing effects of senescence-inducing agents or genetic depletion of *Crtc2* on BCAA catabolic pathway as well as cellular senescence. **d**. QPCR analysis showing effects of senescence-inducing agents or genetic depletion of *Crtc2* on *Il1b* expression. Data represent mean ± SEM (n = 3 biological replicates per group, except control condition of *Crtc2* AKO group, where n = 2 biological replicates were used). **e**. Effects of ADCM (induced by senescence-inducing agent bleomycin) on cellular senescence of AP cells from *Crtc2* f/f mice or *Crtc2* AKO mice were analyzed. Cells were treated with either control ADCM or ADCM from adipocytes treated with bleomycin, with or without anti-IL-1β antibody or anti-TNF-α antibody for 6 days. To induce adipogenic differentiation, cells were incubated with insulin and rosiglitazone for 5 days, and then stained with oil red O staining. A representative data was shown (scale bars, 150 μm). *P* values were determined using student's t-test.

https://doi.org/10.1038/s43587-023-00460-8

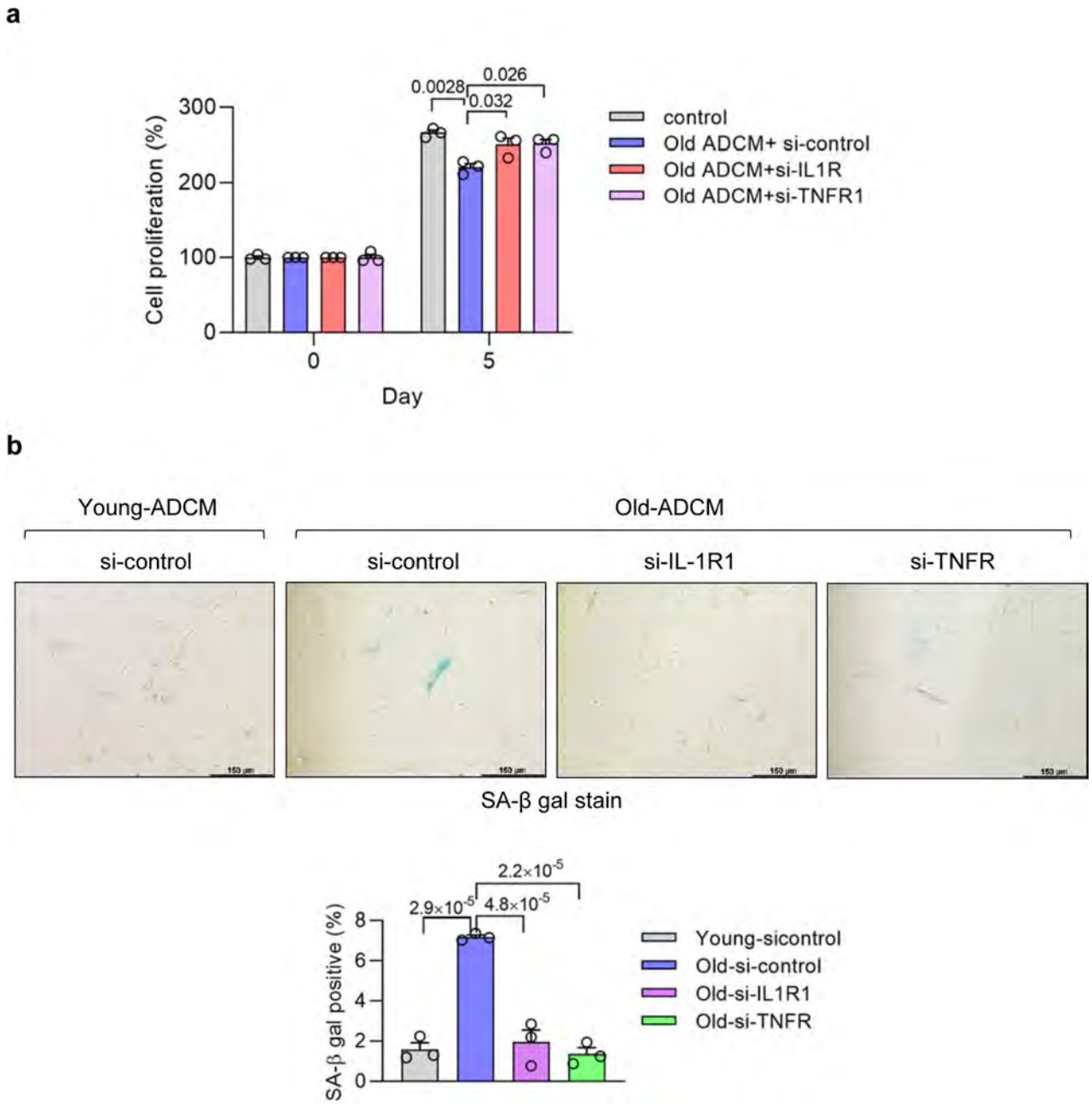

Extended Data Fig. 10 | Role of SASP receptors of adipocytes in age-mediated cellular senescence. a. Effects of ADCM on cell proliferation of AP cells from WT mice were analyzed. Cells were transfected with control siRNA, siRNA against TNFR1, or siRNA against IL1R1, and then treated with either control ADCM or ADCM from old mice for 5 days. Cell proliferation was assessed every 2 days after plating using the CyQuant assay. Data represent mean ± SEM (n = 3 biological replicates per group). **b**. Effects of ADCM on cellular senescence of AP cells from WT mice were analyzed. Cells were transfected with control siRNA, siRNA against TNFR, or siRNA against IL-1R, and then treated with either control ADCM or ADCM from old mice for 5 days. SA-β-gal staining was performed for detecting cellular senescence. A representative image was shown (scale bars, 150 μm). Relative values for SA-β-gal positive cells were also shown. Data represent mean ± SEM (n = 3 biological replicates per group). *P* values were determined using one-way ANOVA with Tukey's multiple comparisons test.

nature portfolio

Corresponding author(s): Seung-Hoi Koo

Last updated by author(s): May 30, 2023

Reporting Summary

Nature Portfolio wishes to improve the reproducibility of the work that we publish. This form provides structure for consistency and transparency in reporting. For further information on Nature Portfolio policies, see our Editorial Policies and the Editorial Policy Checklist.

Statistics

For all statistical analyses, confirm that the following items are present in the figure legend, table legend, main text, or Methods section.

n/a	Confirmed
☐	☒ The exact sample size (*n*) for each experimental group/condition, given as a discrete number and unit of measurement
☐	☒ A statement on whether measurements were taken from distinct samples or whether the same sample was measured repeatedly
☐	☒ The statistical test(s) used AND whether they are one- or two-sided *Only common tests should be described solely by name; describe more complex techniques in the Methods section.*
☐	☒ A description of all covariates tested
☐	☒ A description of any assumptions or corrections, such as tests of normality and adjustment for multiple comparisons
☐	☒ A full description of the statistical parameters including central tendency (e.g. means) or other basic estimates (e.g. regression coefficient) AND variation (e.g. standard deviation) or associated estimates of uncertainty (e.g. confidence intervals)
☐	☒ For null hypothesis testing, the test statistic (e.g. *F*, *t*, *r*) with confidence intervals, effect sizes, degrees of freedom and *P* value noted *Give P values as exact values whenever suitable.*
☒	☐ For Bayesian analysis, information on the choice of priors and Markov chain Monte Carlo settings
☒	☐ For hierarchical and complex designs, identification of the appropriate level for tests and full reporting of outcomes
☒	☐ Estimates of effect sizes (e.g. Cohen's *d*, Pearson's *r*), indicating how they were calculated

Our web collection on statistics for biologists contains articles on many of the points above.

Software and code

Policy information about availability of computer code

Data collection	Leica Application suite X(3.7.0.20979) was used for IHC or fluorescence image acquisition. LSM 700/800 ZEN 2.1 system was used for confocal image acquisition. Bio-Rad CFX Magnager 3.0 software was used for Q-PCR analysis. BioTek Synergy HT Gen5 v2.01 software was used to detect fluorescence signal of microplate.
Data analysis	ImageJ(NIH)1.53c was used for western band intensity analysis. Graphpad prism 8.3.0 and SPSS software version 24.0 were used for statistical analysis. The MassHunter Workstation (Ver B.06.00; Agilent Technologies) was used for data acquisition and analysis. The spectral data were processed by MarkerViewTM (Ver 1.3.1; AB Sciex) software to find peaks, to perform the alignment, and to generate peak tables made of m/z and retention times Automated annotation was performed through the annotation pipeline in MS-DIAL (Ver 3.90), followed by manual confirmation procedure. PCA analysis for liver lipidomics was PCA Minitab 17 software. To capture the overall trend in our multi-omics data, descriptive statistical analysis and PCA analysis was conducted in R (v.4.2.1). Hypergeometric tests were conducted to find significantly enriched pathways in GO database using goseq R package (v.1.52.0). For color coding of KEGG pathway, Pathview R package (1.40.0) was used. Raw reads for scRNA-seq were mapped to the mouse reference genome (GRCm38) and processed using the Cell Ranger software (v3.0.2). Droplets containing cells were identified using DropletUtils (v1.61) R package. To filter out low-quality cells, cells with > 10% of UMIs assigned to mitochondrial genes and less than 2.5 log10-scaled total UMI count were excluded using the calculateQCMetrics function of the scater (v1.14.6) R package. Cells were clustered using the quickCluster function of the scran (v1.0.2) R package and cell-specific size factors were calculated using the computeSumFactors function of the same package.

All cells were clustered into 35 clusters using the FindClusters function of the Seurat (v3.1.5) R package.
Odds ratios and associated p-values of cell type proportion changes between conditions were evaluated with the mixed effect models using the glmer function of the lme4 (v.1.1.25) R package.
The pseudotime analysis was performed using the Palantir (v0.2.6) python package.
GO enrichment analysis was performed using the runTest function of the topGO (v.2.38.1) R package.
The activity of signaling pathways for each stage was inferred using the progeny function of the progeny (v.1.12.0) R package.
Ligand-receptor analysis was conducted using the CellphoneDB (v.2.0.0) python package.

For manuscripts utilizing custom algorithms or software that are central to the research but not yet described in published literature, software must be made available to editors and reviewers. We strongly encourage code deposition in a community repository (e.g. GitHub). See the Nature Portfolio guidelines for submitting code & software for further information.

Data

Policy information about availability of data

All manuscripts must include a data availability statement. This statement should provide the following information, where applicable:

- Accession codes, unique identifiers, or web links for publicly available datasets
- A description of any restrictions on data availability
- For clinical datasets or third party data, please ensure that the statement adheres to our policy

All the data supporting this work are available as Source Data or Supplementary Information. The data for the mRNA-seq and scRNA-seq were deposited in the National Cancer Center for Biotechnology Information (accession number: GSE207433 (for mRNA-seq), PRJNA852570 (for scRNA-seq)). Processed data for mRNA-seq was also deposited in the same location. Processed data for the scRNA-seq is available at https://doi.org/10.5281/zenodo.7949695. Analysis scripts for scRNA-data is available at https://github.com/CB-postech/NATURE-AGING-adipose-CRTC2.
MS/MS patterns from features were identified by comparing the experimental data against METLIN (metlin.scripps.edu) database, and Kyoto Encyclopedia of Genes and Genomes (KEGG, https://www.genome.jp/kegg/) database was used to integrate multi-omics profiles.

Research involving human participants, their data, or biological material

Policy information about studies with human participants or human data. See also policy information about sex, gender (identity/presentation), and sexual orientation and race, ethnicity and racism.

Reporting on sex and gender	N/A
Reporting on race, ethnicity, or other socially relevant groupings	N/A
Population characteristics	N/A
Recruitment	N/A
Ethics oversight	N/A

Note that full information on the approval of the study protocol must also be provided in the manuscript.

Field-specific reporting

Please select the one below that is the best fit for your research. If you are not sure, read the appropriate sections before making your selection.

☒ Life sciences ☐ Behavioural & social sciences ☐ Ecological, evolutionary & environmental sciences

For a reference copy of the document with all sections, see nature.com/documents/nr-reporting-summary-flat.pdf

Life sciences study design

All studies must disclose on these points even when the disclosure is negative.

Sample size	No sample size calculation was performed. Sample size was determined based on the previously published results (Ref 16-18), based on the cost of experiment, feasibility of the experiment, as well as the availability of age-matched mice from each genotype.
Data exclusions	No data were excluded from the analyses.
Replication	Findings were replicated and reproduced at least three independent experiments with biological replicates. All experimental findings were reproducible.
Randomization	The littermate mice were selected for each experimental condition.
Blinding	Blinding was not relevant since equal experimental parameters were consistently applied for each sample during data acquisition

Blinding | and data analysis. No subjective measures were used.

Reporting for specific materials, systems and methods

We require information from authors about some types of materials, experimental systems and methods used in many studies. Here, indicate whether each material, system or method listed is relevant to your study. If you are not sure if a list item applies to your research, read the appropriate section before selecting a response.

Materials & experimental systems

n/a	Involved in the study
☐	☒ Antibodies
☒	☐ Eukaryotic cell lines
☒	☐ Palaeontology and archaeology
☐	☒ Animals and other organisms
☒	☐ Clinical data
☒	☐ Dual use research of concern
☒	☐ Plants

Methods

n/a	Involved in the study
☒	☐ ChIP-seq
☒	☐ Flow cytometry
☒	☐ MRI-based neuroimaging

Antibodies

Antibodies used

Anti-p-CREB: (Rockland, 600-401-270, polyclonal rabbit IgG, 1:2000)
Anti-CREB: (Cell signaling, 9197, monoclonal rabbit IgG, 1:2000)
Anti-p-p70S6K(T389): (cell signaling, 9205, polyclonal rabbit IgG, 1:5000)
Anti-p-p70S6K(T389): (Cell signaling, 9234, monoclonal rabbit IgG, 1:5000)
Anti-p70S6K: (Cell signaling, 9202, polyclonal rabbit IgG, 1:5000)
Anti-p-AMPKa(T172): (Cell signaling, 2535, monoclonal rabbit IgG, 1:5000)
Anti-AMPK: (Cell signaling, 2532, polyclonal rabbit IgG, 1:5000)
Anti-SIRT1: (Millipore, 07-131, polyclonal rabbit IgG, 1:5000)
Anti-β-actin: (Sigma, A5441, monoclonal mouse IgG, 1:5000)
Anti-F4/80: (Cell signaling, 70076, monoclonal rabbit IgG, 1:200)
Anti-Crtc2: (Calbiochem, ST1099, polyclonal rabbit IgG, 1:5000)
Anti-Hsp90: (Santa Cruz Biotechnology, sc-13119, monoclonal mouse IgG, 1:5000)
Anti-α-tubulin: (Sigma, T5168, monoclonal mouse IgG, 1:5000)
Anti-GAPDH: (Santa Cruz Biotechnology, Sc-25778, polyclonal rabbit IgG, 1:5000)
PE-anti-mouse CD140a: (Biolegend, 135905, monoclonal rat IgG, 10ul)
Anti-p-AKT(S473): (Cell signaling, 9271, polyclonal rabbit IgG, 1:5000)
Anti-p-AKT(T308): (Cell signaling, 9275, polyclonal rabbit IgG, 1:5000)
Anti-p-IR(Y1162/1163): (Calbiochem, 407707, polyclonal rabbit IgG, 1:2000)
Anti-AKT: (Cell signaling, 9272, polyclonal rabbit IgG, 1:5000)
Anti-IR: (Santa Cruz Biotechnology, sc-711, polyclonal rabbit IgG, 1:2000)
Anti-PPARg: (Cell signaling, 2435, monoclonal rabbit IgG, 1:5000)
Anti-p21: (Abcam, ab188224, monoclonal rabbit IgG, 1:5000)
Anti-Hes1: (Cell signaling, 11988, monoclonal rabbit IgG, 1:5000)
Anti-γ-H2AX: (Cell signaling, 9718, monoclonal rabbit IgG, 1:200)
Anti-BCKDHA: (Santa Cruz Biotechnology, Sc-271538, monoclonal mouse IgG, 1:5000)
Anti-BCKDHB: (Santa Cruz Biotechnology, sc-374630, monoclonal mouse IgG, 1:5000)
Anti-BCAT2: (Proteintech, 16417-1-AP, polyclonal rabbit IgG, 1:5000)
TNFα neutralizing Ab: (Cell signaling, 11969, monoclonal rabbit IgG, 10ng/ml)
IL-1β neutralizing Ab: (R&D systems, AF-401-NA, polyclonal goat IgG, 10ng/ml)

Validation

Anti-p-CREB: (suitable for WB, ELISA; reacts with human, mouse, rat; https://www.rockland.com/categories/primary-antibodies/creb-phospho-s133-antibody-600-401-270/)
Anti-CREB: (suitable for WB, IP, IHC; reacts with human, mouse, rat, monkey, D.melanogaster; https://www.cellsignal.com/products/primary-antibodies/creb-48h2-rabbit-mab/9197)
p-p70S6K(T389): (suitable for WB; reacts with human, mouse, rat, monkey; https://www.cellsignal.com/products/primary-antibodies/phospho-p70-s6-kinase-thr389-antibody/9205)
p-p70S6K(T389): (suitable for WB; reacts with human, mouse, rat, monkey; https://www.cellsignal.com/products/primary-antibodies/phospho-p70-s6-kinase-thr389-108d2-rabbit-mab/9234)
p70S6K: (suitable for WB, IP; reacts with human, mouse, rat, monkey; https://www.cellsignal.com/products/primary-antibodies/p70-s6-kinase-antibody/9202)
p-AMPKa(T172): (suitable for WB, IP, IHC; reacts with human, mouse, rat, monkey; https://www.cellsignal.com/products/primary-antibodies/phospho-ampka-thr172-40h9-rabbit-mab/2535)
AMPK: (suitable for WB, IP; reacts with human, mouse, rat, hamster, monkey; https://www.cellsignal.com/products/primary-antibodies/ampka-antibody/2532)
SIRT1: (suitable for ChIP, ICC, WB; reacts with human, mouse; https://www.merckmillipore.com/KR/ko/product/Anti-Sirt1Sir2-Antibody,MM_NF-07-131)
β-actin: (suitable for WB, IF; reacts with human, bovine, sheep, pig, rabbit, cat, dog, mouse, rat; https://www.sigmaaldrich.com/deepweb/assets/sigmaaldrich/product/documents/296/386/a5441dat.pdf)

Anti-F4/80: (suitable for WB, IP, IHC; reacts with mouse, https://www.cellsignal.com/products/primary-antibodies/f4-80-d2s9r-xp-rabbit-mab/70076)
Anti-Crtc2: (suitable for WB, IP; reacts with human, mouse, rat; https://www.merckmillipore.com/KR/ko/product/Anti-TORC2-454-607-Rabbit-pAb,EMD_BIO-ST1099)
Anti-Hsp90: (suitable for WB, IP, IF, IHC, ELISA, reacts with human, mouse, rat; https://www.scbt.com/p/hsp-90alpha-beta-antibody-f-8)
Anti-α-tubulin: (suitable for WB, ICC, reacts with human, mouse, rat; https://www.sigmaaldrich.com/deepweb/assets/sigmaaldrich/product/documents/371/375/t5168dat.pdf)
Anti-GAPDH: (suitable for WB, IP, IF, IHC, reacts with human, mouse, rat; https://datasheets.scbt.com/sc-25778.pdf)
PE-anti-mouse CD140a: (suitable for FACS, WB, IHC, reacts with mouse; https://www.biolegend.com/en-us/products/pe-anti-mouse-cd140a-antibody-6253)
Anti-p-AKT(S473): (suitable for WB, IP, IF, FACS, reacts with human, mouse, rat; https://www.cellsignal.com/products/primary-antibodies/phospho-akt-ser473-antibody/9271)
Anti-p-AKT(T308): (suitable for WB, IP, reacts with human, mouse, rat; https://www.cellsignal.com/products/primary-antibodies/phospho-akt-thr308-antibody/9275)
Anti-p-IR(Y1162/1163): (suitable for WB, ICC, ELISA, reacts with human; https://www.merckmillipore.com/KR/ko/product/PhosphoDetect-Anti-Insulin-Receptor-pTyr1162-1163-Rabbit-pAb,EMD_BIO-407707)
Anti-AKT: (suitable for WB, IP, IF, FACS, reacts with human, mouse, rat; https://www.cellsignal.com/products/primary-antibodies/akt-antibody/9272)
Anti-IR: (suitable for WB, IP, IF, reacts with human, mouse, rat; https://datasheets.scbt.com/sc-711.pdf)
Anti-PPARg: (suitable for WB, IHC, IF, ChIP, reacts with human, mouse; https://www.cellsignal.com/products/primary-antibodies/pparg-c26h12-rabbit-mab/2435)
Anti-p21: (suitable for WB, IHC, IP, ICC, reacts with mouse; https://www.abcam.com/products/primary-antibodies/p21-antibody-epr18021-ab188224.html)
Anti-Hes1: (suitable for WB, IP, IHC, reacts with human, mouse, rat; https://www.cellsignal.com/products/primary-antibodies/hes1-d6p2u-rabbit-mab/11988)
Anti-γ-H2AX: (suitable for WB, IHC, IF, reacts with human, mouse, rat, monkey; https://www.cellsignal.com/products/primary-antibodies/phospho-histone-h2a-x-ser139-20e3-rabbit-mab/9718)
Anti-BCKDHA: (suitable for WB, IP, IF, IHC, reacts with human, mouse, rat; https://www.scbt.com/ko/p/bckde1a-antibody-h-5)
Anti-BCKDHB: (suitable for WB, IF, IHC, reacts with human, mouse, rat; https://www.scbt.com/p/bckdhb-antibody-h-6?requestFrom=search)
Anti-BCAT2: (suitable for WB, IHC, IF, ELISA, reacts with human, mouse, rat; https://www.ptglab.com/products/BCAT2-Antibody-16417-1-AP.htm#product-information)
TNFa neutralizing Ab: (suitable for neutralization TNFa, reacts with mouse; https://www.cellsignal.com/products/primary-antibodies/mouse-tnf-a-neutralizing-d2h4-rabbit-mab/11969)
IL-1β neutralizing Ab: (suitable for neutralization IL-1b, WB, IHC, ICC, reacts with mouse; https://www.rndsystems.com/products/mouse-il-1beta-il-1f2-antibody_af-401-na)

Animals and other research organisms

Policy information about studies involving animals; ARRIVE guidelines recommended for reporting animal research, and Sex and Gender in Research

Laboratory animals	Mice had free access to food and water and were caged at 22 °C with 12 h light cycles and 50 % humidity were used for the experiments. For the generation of adipocyte-specific Crtc2 KO mice (Crtc2 AKO), Crtc2 floxed mice were crossed with adiponectin-cre transgenic mice.C57BL/6N young (3-to 5-month-old) and old (18- to 21-month-old) male mice were used.
Wild animals	The study did not involve wild animals.
Reporting on sex	We used only male mice for the current study. We stated the information in the Method.
Field-collected samples	The study did not involve samples collected from the field.
Ethics oversight	All animal experiments were performed following the guidelines established by the Korea University Institutional Animal Care and Use committee (KUIACUC-2018-0031).

Note that full information on the approval of the study protocol must also be provided in the manuscript.